Article

Geology and Geochemistry of the Hongnipo Copper Deposit, Southwest China

Wangdong Yang [1], Gongwen Wang [1,2,3,4,*] and Yunchou Xu [1]

[1] School of Earth Sciences and Resources, China University of Geosciences, Beijing 100083, China
[2] Frontiers Science Center for Deep-time Digital Earth, China University of Geosciences, Beijing 100083, China
[3] MNR Key Laboratory for Exploration Theory & Technology of Critical Mineral Resources, China University of Geosciences, Beijing 100083, China
[4] Beijing Key Laboratory of Land and Resources Information Research and Development, Beijing 100083, China
[*] Correspondence: gwwang@cugb.edu.cn

Abstract: The Hongnipo deposit, a newly discovered large copper deposit in the Kangdian Fe-Cu metallogenic belt of southwest China, is hosted in the Paleoproterozoic metavolcanic and metasedimentary rocks of the Hekou group. The deposit comprises five strata-bound ore bodies and is associated with sporadically distributed gabbroic intrusions. Four stages of mineralization and alteration have been identified: sodic alteration (I), banded sulfide (II), magnetite (III), and sulfide vein/stockwork (IV). Extensive sodic alteration of stage I is confirmed by the composition of feldspars. Trace element analysis of magnetite suggests a formation temperature of 400 ± 50 °C and has a characteristic of IOCG deposits, while high $\delta^{18}O$ values (8.3–11.0‰) of fluids from stage III indicate a magmatic water origin. Sulfide $\delta^{34}S_{VCDT}$ values from stages II and IV range from -2.6 to 10.9‰ and -1.5 to 9.9‰, respectively, suggesting a mixed sulfur source from magmatic H_2S and reduced seawater sulfate. Chalcopyrite from Hongnipo shows a narrow $\delta^{65}Cu$ range of -0.135 to 0.587‰, indicating formation at high temperatures. The lack of correlation between $\delta^{65}Cu$ and $\delta^{34}S_{VCDT}$ values suggests distinct geochemical behaviors in mineralization. In summary, the Hongnipo deposit is classified as a Cu-rich section of a typical IOCG deposit.

Keywords: Hongnipo deposit; stratabound ores; sodic alteration; mineral chemistry; stable isotopes

1. Introduction

The Kangdian region in southwest China hosts numerous Fe-Cu deposits, forming a Precambrian Fe-Cu metallogenic belt [1–4]. These deposits, known for their high grades and unique strata-bound ore bodies, have attracted considerable interest from geologists. Representative deposits such as Lala, Dahongshan, Xikuangshan, and Yinachang have been extensively studied [1–4]. Notably, the Hongnipo is a recently discovered large copper deposit located approximately 5 km south of the Lala Fe-Cu deposit in the northern part of the Kangdian region. The Hongnipo deposit contains approximately 41.6 million tons (Mt) of ore with an average grade of 1.42 wt.% Cu [5] and occurs in a stratigraphic formation different from the Lala deposit.

Understanding the geological characteristics of the Hongnipo deposit is essential due to its unique stratigraphic setting and significant resource potential. Recent studies have provided valuable insights into various aspects of the deposit. Lin et al. (2020) [6] identified two mineralization stages: early laminated ores with a pyrite Rb-Sr isochron age of 1552 ± 80 Ma, likely from a VMS mineralization, and late vein-type ores with a chalcopyrite Re-Os isochron age of 798.8 ± 7.9 Ma, possibly related to Neoproterozoic magmatism and/or metamorphism. Yang et al. (2020) [7] utilized three-dimensional geological modeling to show that the Hekou Group underwent two major tectonic movements, resulting in the current tectonic framework. Furthermore, Lin et al. (2020) [8] revealed a close association of Cu with Ag, Co, Mo, As, and Sb through drill core sample analysis. Song

et al. (2023) [9] analyzed fluid inclusions in sulfide veins, finding them mainly composed of H_2O, CO_2, and minor CH_4, with a wide range of homogeneous temperatures (10.6 to 500 °C) and salinities (8.8 to 59.8‰).

Despite significant progress, several important scientific questions remain unresolved regarding the Hongnipo deposit. First, the precise stratigraphic and lithologic context of the deposit is still poorly understood. Additionally, the paragenetic sequence of alteration and mineralization requires detailed clarification to determine how they compare to other deposits in the region. Furthermore, the sources of ore-forming fluids remain speculative, which is important in classifying the deposit types. These uncertainties highlight the necessity for a comprehensive study focused on these aspects.

This study aims to investigate the host rocks, gabbroic intrusions, paragenetic sequence, and mineralization styles of the Hongnipo deposit. We utilized mineral compositions to identify alteration types and calculate formation temperatures [10] and employed O, S, and Cu isotopes to investigate the origin of ore fluids. Comparisons with other deposits have been made to classify the Hongnipo deposit type. Gaining a comprehensive understanding of the geology and origin of the Hongnipo deposit not only contributes to the scientific knowledge of Fe-Cu deposits in the Kangdian region but also has significant implications for mineral exploration.

2. Regional Geology

The Yangtze Block, located in the northwest part of South China, is bounded by the Tibetan Plateau to the west and the Indochina Block to the southwest (Figure 1A). It is separated from the North China Craton by the Qinling–Dabie orogenic belt. The Yangtze and Cathaysia Blocks amalgamated along a northeast–southwest trending tectonic zone known as the Jiangnan–Shaoxing suture or Jiangnan orogen around 830 Ma [11–13]. Limited Archean rocks are exposed at the northern margin of the Yangtze block, represented by the >3.2 Ga Kongling complex [14].

In the western Yangtze Block, the Kangdian region displays an N-S-oriented fault corridor known as the Kangdian Rift Valley (Figure 1B). This region is characterized by a succession of Neoproterozoic volcanic rocks, ranging from basalts to rhyolites [15,16]. Moving southward, Paleoproterozoic strata like the Dahongshan, Hekou, and Dongchuan groups are widespread (Figure 1B). With an east–west strike, these groups are recognized as lateral equivalents [17–19]. The Dahongshan and Hekou groups, with volcanic rocks ~1.7 Ga, have undergone metamorphism ranging from upper greenschist to lower amphibolite facies [20]. In contrast, the Dongchuan group, deposited between 1.7 and 1.5 Ga [18], consists of various sedimentary rocks and experienced low-grade greenschist metamorphism [21].

The Paleoproterozoic strata are unconformably overlain by late Mesoproterozoic to early Neoproterozoic Kunyang, Huili, and Julin groups [18,22]. The zircon U-Pb ages of metavolcanic rocks in the Kunyang and Huili groups are ~1.0 Ga [23,24]. The metabasalts in the Julin Group have an age of ~1050 Ma [25]. These groups are subsequently covered by diverse Neoproterozoic to Permian strata comprising clastic, carbonate, and volcanic rocks [19].

Intruding the Paleoproterozoic strata are numerous gabbroic and minor granitic rocks (Figure 1B). Within the Dahongshan and Hekou Groups, the formation of gabbroic intrusions and volcanic rocks occurred approximately simultaneously (~1.7 Ga), and they are spatially closely associated with copper deposits [4,26]. In the Yimin Formation at the base of the Dongchuan Group, ~1.7 Ga gabbroic intrusions are considered to be associated with mantle plumes and continental rifts [18].

The Kangdian region is characterized by numerous Fe-Cu deposits within the Paleoproterozoic strata (Figure 1B). Lala, Xikuangshan, Yinachang, Dahongshan, and Hongnipo are the most significant deposits [1–4,27]. These deposits contain irregular, stratigraphically controlled replacement ore bodies or hydrothermal breccias. The dominant ore minerals are Fe-oxides (magnetite and hematite) and/or Cu-sulfides (chalcopyrite and bornite),

with variable amounts of Au, Ag, Co, and REE [28]. Furthermore, the widespread pre-ore albitization and close association with brecciation and contemporaneous mafic intrusions are common features in IOCG deposits.
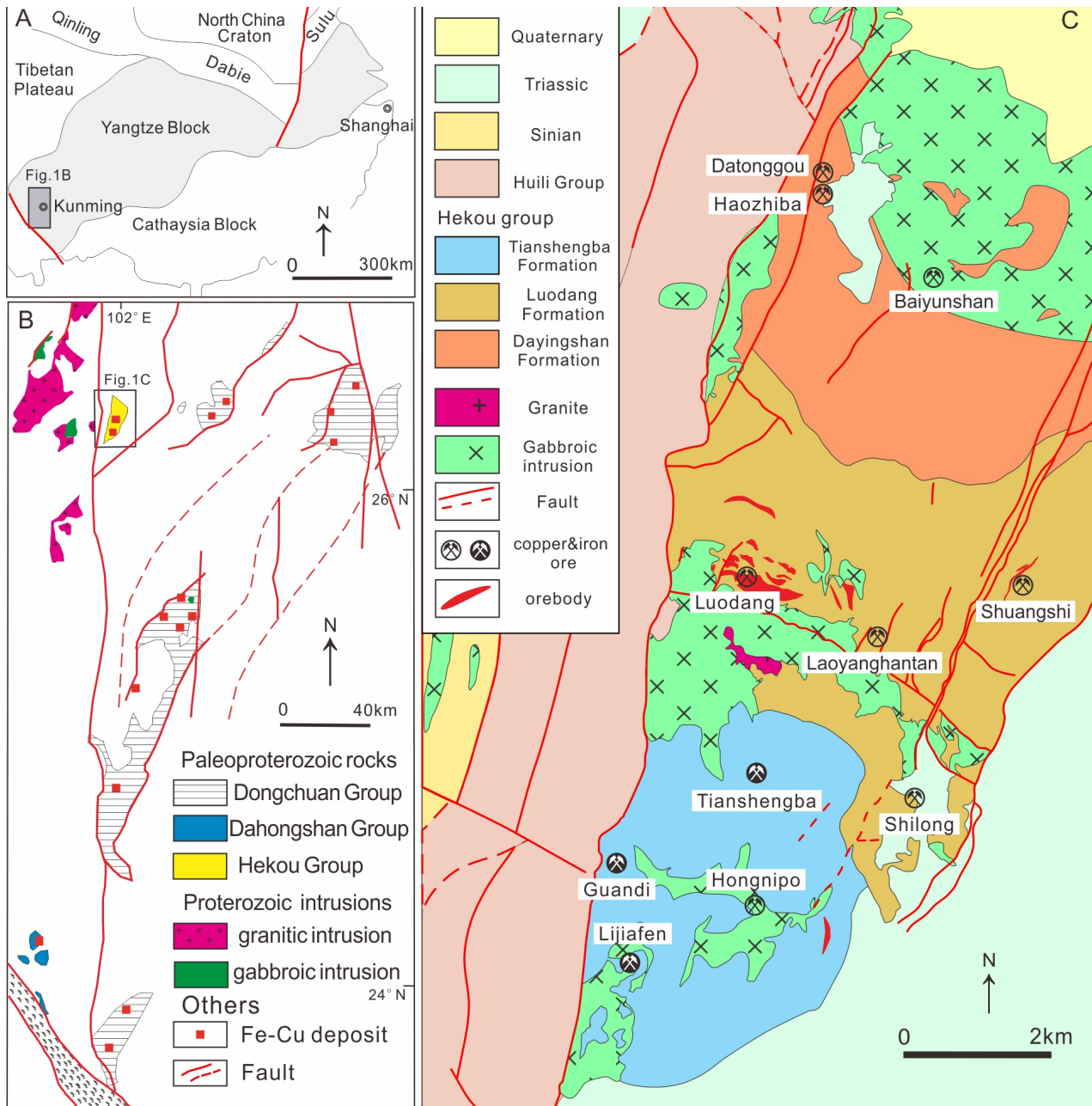

Figure 1. (**A**) Simplified tectonic map showing the location of the Kangdian region in the Yangtze block. (**B**) Regional geologic map of the Kangdian region highlighting the distribution of Fe-Cu deposits, Paleoproterozoic strata, and plutons (after Zhao et al., 2017) [4]. (**C**) Geologic map of the Lala ore camp, showing the distribution of Cu (or Fe) ore deposits and occurrences within the Hekou group, along with their close spatial relationships with gabbroic intrusions (after Gong et al., 2016) [5].

3. Deposit Geology

The Hongnipo deposit is situated at the intersection of NNE- and NW-trending structures (Figure 1C).

3.1. The Hekou Group

The Hekou Group comprises metamorphosed volcanic and sedimentary rocks [26,29]. Within the Hongnipo mining area, drilling has revealed three formations of the Hekou Group: The Tianshegnba, Xinqiao, and Luodang Formations (Figure 2B). The Tianshengba and Luodang Formations are further subdivided into upper and lower members, distinguished by lithological variations and ore-bearing layers.
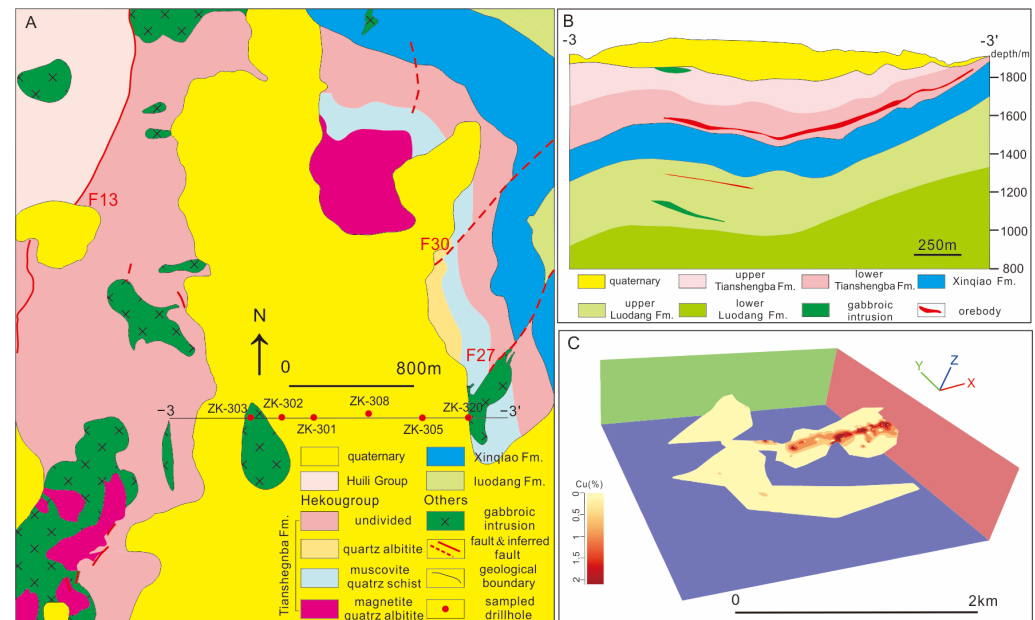

Figure 2. Geologic map (**A**) and cross-section (**B**) of the Hongnipo deposit (after Gong et al., 2016) [5]. (**C**) A three-dimensional model of orebody No. I, including a visualization of the copper grade distribution within the orebody.

The upper Tianshengba Formation is primarily composed of biotite–albite schist, biotite–quartz–albite schist, two-mica-quartz schist, and quartz albitite (Figure 3A,J). There are local occurrences of magnetite lenses within the member. Hydrothermal breccia is also found in specific areas (Figure 3L). Diabase is sparsely distributed near the surface, with the original fabric blurred by intense alteration (Figure 4A). Carbonatization, including sideritization and dolomitization, is extensively developed (Figure 3J). In the lower Tianshengba Formation, the upper portion is mainly composed of biotite–quartz schist, quartz albitite, and phengite–albite schist, with laminated magnetite. The lower portion primarily consists of phengite–quartz–albite schist, porphyritic quartz albitite, phengite–quartz schist, ankerite marble, and biotite–albite schist, with intercalations of carbonaceous slate (Figure 3E–I). The presence of slate and schist suggests possible regional metamorphism [30]. Most ore bodies are hosted in this member (Figure 2C). Chalcopyrite, intergrown with pyrite, occurs as laminae, bands, and veinlets hosted in marble, albitite, and schist. Sideritization, iron dolomitization, and chloritization occur extensively.

The Xinqiao Formation conformably underlies the Tianshengba Formation and consists of biotite–almandine–albite schist, biotite–quartz schist, and biotite albitite (Figure 3B,K). This formation is characterized by the widespread occurrence of almandine and biotite, hence containing a higher Fe content than other formations [8].

The upper Luodang Formation comprises various rock types, including porphyritic albitite, phengite–quartz schist, phengite–albite schist, biotite–albite schist, two-mica-albite schist, albite–amphibole–chlorite schist, and almandine–albite schist (Figure 3C). Intercalated within these rocks are layers of dolomite marble, carbonaceous slate, and sericite–quartz phyllite. Copper ore bodies in this member are stratigraphically controlled. It is the primary ore-bearing member in the Lala deposit and a secondary mineralized zone of

the Hongnipo mining area (Figures 1C and 2B). Carbonatization and chloritization are the major alteration types. The lower Luodang Formation is poorly exposed by drilling, which contains phengite–quartz albitite, phengite albitite, and biotite–quartz schist (Figure 3D).
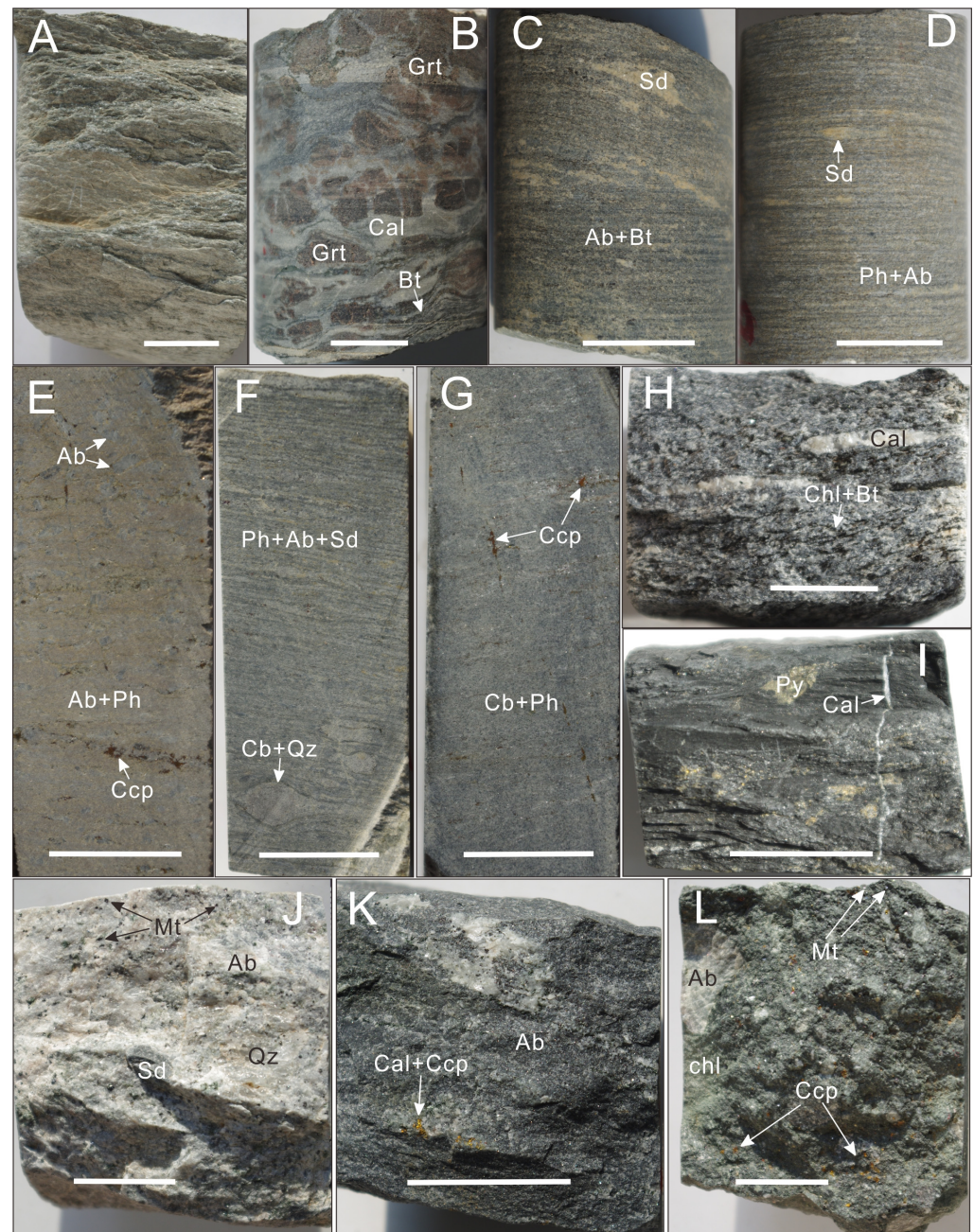

Figure 3. General aspects of the host rocks of the Hongnipo deposit, Hekou group. (**A**) Phengite schist, UTSBF. (**B**) Biotite-garnet schist with strong carbonatization, XQF. (**C**) Biotite–albite schist with lens-shaped siderite, ULDF. (**D**) Siderite–phengite schist with lens-shaped siderite, LLDF. (**E**) Phengite–albite schist featuring white albite porphyroblasts aligned with the foliation, with little chalcopyrite replacing them locally, LTSF. (**F**) Albite–phengite schist with porphyroblasts composed of carbonate and quartz, LTSBF. (**G**) Phengite marble with discontinuous chalcopyrite veins crosscutting and chalcopyrite grains disseminated along the foliation, LTSBF. (**H**) Biotite–albite schist with biotite replaced by chlorite and containing lens-shaped calcite, LTSBF. (**I**) Carbonaceous phyllite with quartz and carbonate mineral lenses, accompanied by pyrite, LTSBF. (**J**) Albitite with disseminated magnetite and irregular siderite alteration, UTSBF. (**K**) Porphyritic albitite with calcite–chalcopyrite veins, XQF.

(**L**) Breccia with fragments of albite and coarse-grained albite grains embedded in a chloritized matrix containing disseminated magnetite and chalcopyrite, UTSBF. The short lines in the diagram represent 2 cm. Abbreviations: Grt = garnet, Cal = calcite, Bt = biotite, Sd = siderite, Ab = albite, Ph = phengite, Ccp = chalcopyrite, Cb = carbonate mineral, Q = quartz, Cal = calcite, Chl = chlorite, Mt = magnetite, UTSBF = Upper Tianshengba formation, LTSBF = Lower Tianshengba formation, XQF = Xinqiao formation, ULDF = Upper Luodang formation, LLDF = Lower Luodang formation.
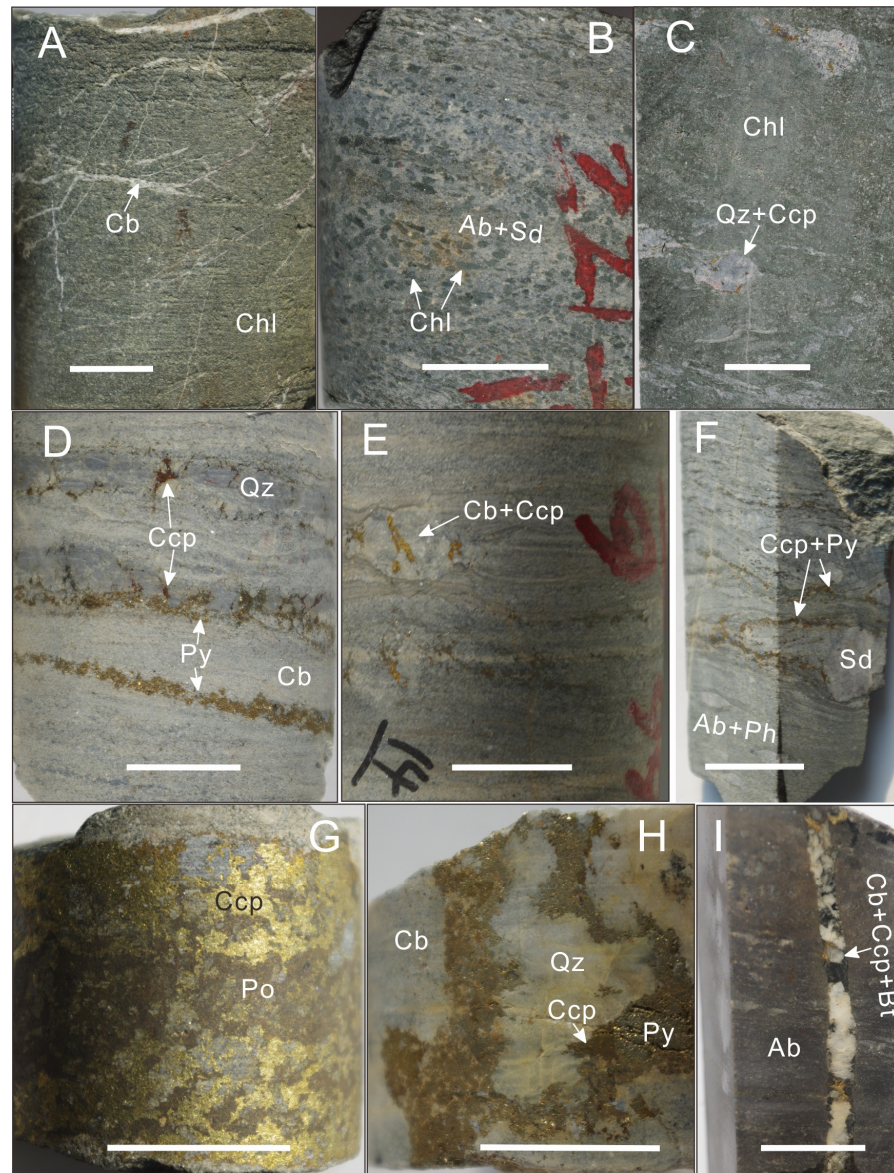

Figure 4. Gabbroic rocks and various sulfide ores of the Hongnipo deposit. (**A**) Metadiabase, with most mafic minerals altered to chlorite and crosscut by carbonate veinlets, UTSBF. (**B**) Metagabbro with medium-sized, platy chlorite grains oriented along the foliation and a matrix composed of fine-grained albite aggregates, exhibiting widespread siderization, LTSBF. (**C**) Metagabbro with lens-shaped intergrowths of quartz–chalcopyrite and widespread chloritization, LTSBF. (**D**) Banded sulfide ore featuring euhedral pyrite aggregates aligned with the foliation, with anhedral chalcopyrite aggregates filling the gaps between quartz and pyrite grains within the marble. (**E**) Sulfide ore with an augen structure composed of carbonate and chalcopyrite. (**F**) Sulfide ore with laminated sulfides surrounding the siderite porphyblasts and the matrix composed of albite and phengite. (**G**) Massive ore with chalcopyrite infilled and replaced by pyrrhotite. (**H**) Quartz–sulfide vein within the marble. (**I**) Carbonate-chalcopyrite-biotite vein crosscutting the albite schist. The short lines in the diagram represent 2 cm. Abbreviations: Py = pyrite, Po = pyrrhotite; see Figure 3 for the remainder.

3.2. Gabbroic Intrusions

Gabbroic intrusions occur sporadically in both the Tianshengba and Luodang Formations, and various degrees of alteration and metamorphism have been identified (Figures 1C, 4A–C and 5A–C,K). Pyroxene is wholly or partially altered to hornblende, chlorite, and biotite, while plagioclase is extensively replaced by albite. Gabbroic rocks in the borehole exhibit a discontinuous distribution, complicating their spatial morphology identification. However, the oriented arrangement of the minerals suggests that these rocks' distribution is likely aligned with the bedding (Figures 2B and 5C,K). Different intrusion depths result in vertical variations in the texture of gabbroic rocks.
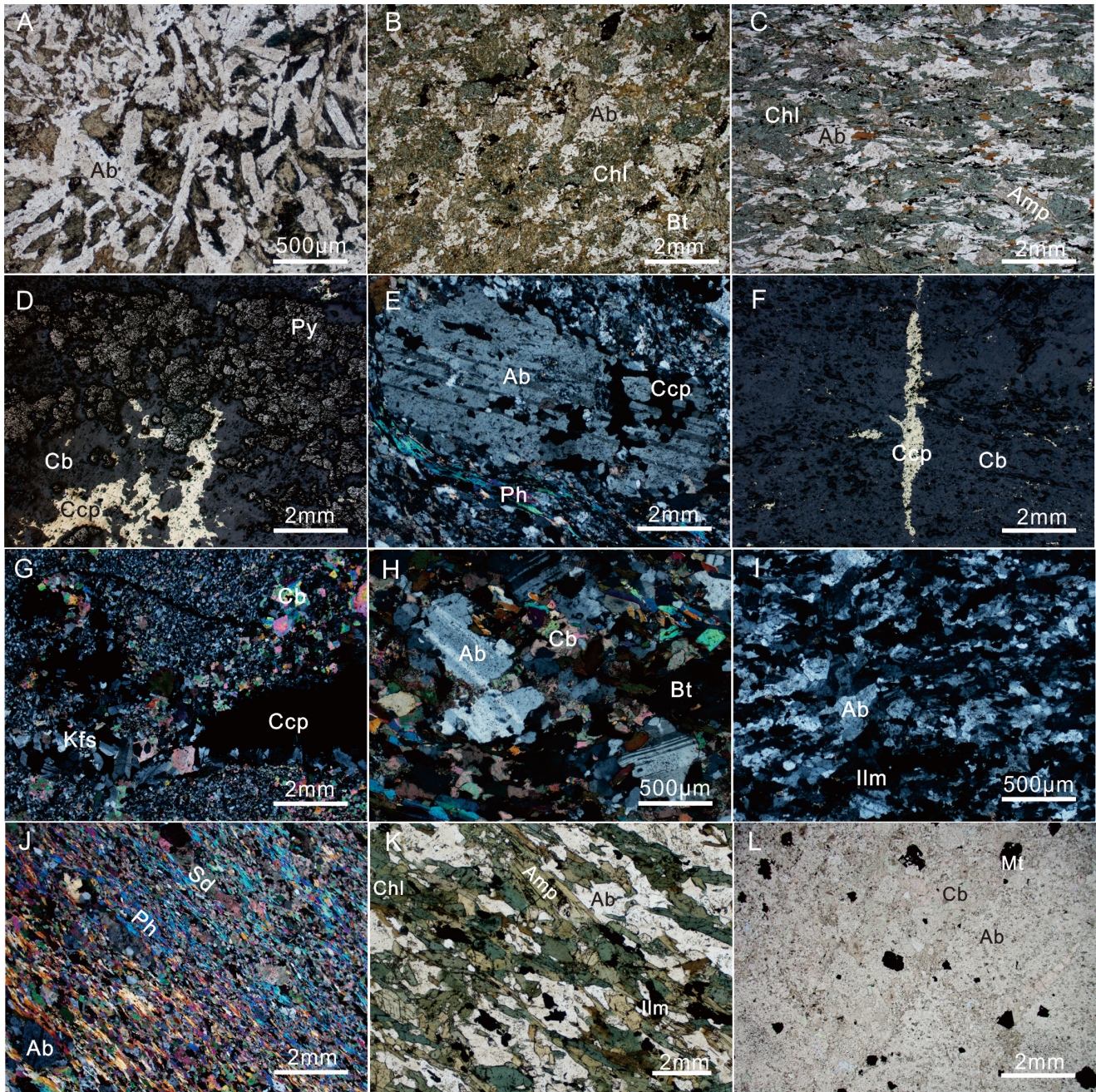

Figure 5. Photomicrographs of gabbroic rocks, sulfide ores, and various altered rocks. (**A**) Metadiabase, typical ophitic texture, with tabular plagioclase grains filled by mafic minerals, UTSBF. (**B**) Metagabbro

with the original magmatic fabric virtually obliterated, ULDF. (**C**) Metagabbro, platy chlorite, and minor biotite oriented along the foliation, LLDF. (**D**) Subhedral pyrite aggregates infilled by anhedral chalcopyrite within banded sulfide ore. (**E**) Albite porphyroblast with a rough surface and replaced by chalcopyrite. (**F**) Chalcopyrite occurs as veins crosscutting or disseminated grains parallel to the foliation. (**G**) Carbonate–chalcopyrite–K-feldspar veins. (**H**) Albite grains with a rough surface, surrounded and replaced by carbonate minerals. (**I**) Sodic alteration, mainly composed of albite with minor ilmenite. (**J**) Schist with porphyroblasts composed of albite and siderite surrounded by platy phengite. (**K**) Amphibole and chlorite distributed parallel to the foliation and intergrown with ilmenite. (**L**) Euhedral magnetite distributed in carbonatization albitite. Abbreviations: Amp = amphibole, Py = pyrite, Kfs = K-feldspar; see Figure 4 for the remainder.

Diabase is the dominant mafic phase in the upper Tianshengba Formation, which is crosscut by abundant carbonate (-hematite) veins (Figures 4A and 5A). In the lower Tianshengba Formation, gabbroic intrusions are strongly altered; chlorite, hornblende, biotite, and saponite constitute the main mafic minerals. The matrix consists of fine-grained albite infilled by carbonate minerals (Figure 4B). In intensely foliated rocks, residual albite porphyroblasts are surrounded by oriented chlorite and biotite. Local lenses of quartz are closely associated with magnetite, chalcopyrite, and minor bornite (Figure 4C).

The gabbroic rocks intruding into the Luodang Formation exhibit a zircon U-Pb age of ~1.7 Ga [26], showing temporal correlation with the metavolcanic rocks of the strata. Gabbro dominates the upper Luodang Formation; the original magmatic fabric is virtually obliterated, with isotropic mineral assemblages consisting of mafic minerals and faintly twinned plagioclase, which have blurred boundaries (Figure 5B). In the lower Luodang Formation, gabbro has coarser mineral grains. Foliation is defined by the alignment of platy chlorite and albite, indicating the significant influence of lithostatic pressure (Figure 5C).

3.3. Copper Mineralization

The Hongnipo deposit comprises five orebodies distributed across a 2.2 km × 2.5 km area. Notably, 98% of the total reserves are concentrated in the No. I Cu orebody [5]. All five orebodies are stratigraphically controlled, located within the metavolcanic and metasedimentary rocks of the Lower Tianshengba and upper Luodang Formations, and exhibit stratiform, stratoid, and lenticular structures (Figure 2B,C).

On plan view, the No. I Cu orebody exhibits an irregular bay-like shape, resembling an arrow pointing westward (Figure 2C). It dips to the northwest at an angle of 10 to 25 degrees, forming an anticline–syncline structure in a northwest-to-southeast direction. This distribution results in the orebody's eastern side being shallow, approximately 60 m below the surface, while its central section is located at a depth of around 400 m. The orebody is thin, with an average thickness of 11.55 m [5]. Such geometrical characteristics play a pivotal role in evaluating and planning mining operations.

The distribution of copper grades in No. I Cu orebody is predominantly influenced by the strike of strata and is closely linked to specific ore types present (Figure 2C). The eastern segment boasts the highest grades, mainly characterized by stockwork ore zones oriented towards the west–northwest. Conversely, regions with fine-grained and weakly altered host rocks exhibit lower copper grades. In a broader context, the disseminated and banded ores have inferior grades compared to their stockwork counterparts. Chalcopyrite with trace amounts of bornite constitutes the main ore minerals commonly associated with pyrite and locally distributed pyrrhotite.

4. Paragenetic Sequence of Alteration and Mineralization

After a complex evolutionary process, the Hongnipo deposit has been characterized by four distinct alteration and mineralization events. The recognized paragenetic sequence comprises the sodic alteration (I), banded sulfide (II), magnetite (III), and late sulfide vein (IV) stages (Figure 6).

Stage / Mineral	Stage I (Sodic alteration)	Stage II (Banded sulfide)	Stage III (Magnetite)	Stage IV (Sulfide vein/stockwork)
Albite	major			
Pyrite		major		major
Chalcopyrite		minor		minor
Pyrrhotite		minor		minor
Bornite		local		local
Quartz		minor	local	major
Magnetite			minor	
K-feldspar				local
Molybdenite				local
Cobaltite				local
Calcite				major
Dolomite				minor
Biotite				local

Figure 6. Simplified paragenetic sequence of alteration and mineralization in the Hongnipo deposit. Thick, thin, and dashed lines represent relative proportions of minerals (major, minor, and local, respectively).

4.1. Sodic Alteration Stage (Stage I)

In the Hongnipo deposit, sodic alteration is widespread and primarily characterized by the occurrence of albite within the host rocks. Coarse albite grains primarily occur as porphyroblasts within various types of schist (Figures 3E and 5E,H). Additionally, abundant fine-grained sodic plagioclase is distributed within the matrix of schist and albitite (Figures 3C,D,F,J,K and 5I). In gabbroic rocks, albite has replaced most of the calcic-bearing plagioclase (labradorite), forming distinctive aggregates dispersed throughout the matrix (Figure 5C). Furthermore, albite occurs as both coarse-grained fragments and fine-grained aggregates within breccia (Figure 3L), suggesting that sodic alteration predates brecciation. Albite is distinguished by its polysynthetic twinning and Carlsbad-albite twinning (Figure 5E,H). It commonly has a rough surface and internally contains numerous inclusions with diameters less than 10 μm. Evident signs of erosion along the edges of these porphyroblasts are indicative of subsequent hydrothermal alteration (Figure 5H). Locally, albite aggregates display a red appearance attributed to iron oxide inclusions [31].

4.2. Banded Sulfide Stage (Stage II)

This stage typically exhibits a confined or oriented mineral assemblage parallel to the foliation. The assemblage is mainly dominated by pyrite, infilled with minor chalcopyrite; other less abundant minerals include quartz, pyrrhotite, and bornite (Figure 6). Sulfide minerals are present in several distinct forms: (1) Laminated or banded aggregates parallel to or oriented along the foliation of the host rocks (Figure 4D,F). (2) Laminated sulfide minerals located at the contact zones between lenses and the matrices (Figure 4F). (3) Disseminated grains enclosing or directly replacing porphyroblasts (e.g., albite, quartz, and carbonate minerals, Figures 4E and 5E).

Pyrite occurs as euhedral to subhedral granular aggregates, while chalcopyrite appears as irregular fillings between subhedral pyrite grains and irregularly occupies interstices among quartz grains (Figures 4D and 5D). In porphyritic albitite, chalcopyrite is commonly found surrounding or replacing albite phenocrysts (Figures 4E and 5E). Furthermore, chal-

copyrite is closely associated with quartz in quartz-bearing marbles (Figure 4D). It occurs as discontinuous veins intersect and as disseminated grains dispersed parallel to the foliation (Figures 3G and 5F). Within the biotite schist, chalcopyrite disseminates throughout the rock and replaces carbonate minerals and biotite along the schistosity. Locally, chalcopyrite occurs as disseminated grains within the breccia matrix (Figure 3L). The host rocks of this mineralization stage mainly consist of marble, followed by mica schist and albitite.

4.3. Magnetite Stage (Stage III)

Magnetite dominates this stage, but it is only locally distributed. It is either disseminated within the matrix of the host rocks or forms lamellae parallel to the foliation and rarely occurs in massive form (Figure 5L). In the matrix, magnetite appears as euhedral to subhedral granular forms, exhibiting square, triangular, or hexagonal shapes in cross-section (Figure 5L). In contrast, anhedral magnetite with quartz forms aggregates in massive ores.

4.4. Sulfide Vein/Stockwork Stage (Stage IV)

The ores of the Hongnipo primarily formed during this mineralization stage. The mineral assemblage of this stage remains largely unmetamorphosed, forming veins or stockworks that cut across former foliated rocks. Local enrichments manifest as massive ores (Figure 4G), which typically exhibit higher copper grades, closely correlating with the distribution of the ore shoot.

Chalcopyrite $\pm$ pyrite $\pm$ magnetite typically forms veins with quartz or calcite, crosscutting the host rocks (Figures 4H,I and 5G). Compared to the banded sulfide stage, it has a higher chalcopyrite/pyrite ratio. Quartz veins have vague boundaries with surrounding rocks, while calcite veins have distinct, straight boundaries with the host rocks (Figure 4H,I). Host rocks are often infilled and replaced by sulfides, resulting in a characteristic triangular-acute angle texture (Figure 4G). In massive ores, sulfides consist of intimately intergrown chalcopyrite, pyrite, and pyrrhotite, with sporadic quartz inclusions forming a metasomatic relict texture (Figure 4G). Locally, chalcopyrite is replaced by bornite. Other minerals present include cobaltite, dolomite, biotite, and K-feldspar (Figure 6).

5. Sampling and Analytical Methods

For petrographic and experimental studies, we collected samples of host rocks and ores from six drill holes (Figure 2A). To enhance the representativeness of the samples for mineral compositional analyses, we selected 61 mineral grains from 28 feldspar samples and 32 mineral grains from 13 magnetite samples. Five samples were used to analyze magnetite oxygen isotopes, and ten were used for sulfur and copper isotopes. To ensure the accuracy of isotope studies, we selected samples that clearly showed only one stage of mineralization under the naked eye, thereby indicating the isotopic composition of that stage. Samples containing two stages of mineralization will be labeled in the table.

5.1. Electron Probe Microanalysis

The compositions of feldspar and magnetite grains were determined using a Shimadzu EPMA-1720 instrument equipped with five wavelength dispersive spectrometers at the Electron Probe Microanalysis (EPMA) Laboratory, China University of Geosciences, Beijing. The rock-thin sections were carbon-coated. A focused beam at an accelerating voltage of 15 keV and a current of 10 nA was used, and the beam diameter was 5 μm. The peak counting times were 10 s for Na, V, Si, Ti, Mg, Ni, K, Cr, Al, Fe, Mn, and Ca and 10 s for the background. Inclusions within minerals were carefully avoided. The intensity data were corrected using the ZAF method.

5.2. Oxygen and Sulfur Isotopes

At the Isotope Laboratory of ALS minerals, oxygen isotope analysis was conducted on magnetite, while sulfur isotope compositions were analyzed on sulfide minerals, including

chalcopyrite, pyrite, and pyrrhotite. Mineral separates were extracted from drill core samples and were ground into 200 meshes.

The sulfur isotopic composition was measured using a MAT 253 Stable Isotope Ratio Mass Spectrometer (Thermo Fisher Scientific, Waltham, MA, USA) coupled to a Costech ECS 4010 Elemental Analyzer (Valencia, CA, USA). $\delta^{34}S$ values were calculated by normalizing the $^{34}S/^{32}S$ ratios in the sample to that in the Vienna Canyon Diablo Troilite (VCDT) international standard; values are reported using the delta (δ) notation in units of per mil (‰) and are reproducible to 0.2 per mil.

Oxygen isotope values were determined using the conventional BrF_5 method described by Clayton and Mayeda (1963) and analyzed with a Finnigan MAT 252 isotope-ratio mass spectrometer (IRMS, Thermo Finnigan LLC., San Jose, CA, USA). Approximately 5 mg of mineral separate underwent BrF_5 treatment at around 550–600 °C overnight. The released oxygen was converted into CO_2 and then analyzed using the same Finnigan MAT 252 IRMS. Results are reported in $\delta^{18}O$ notation relative to the Vienna standard mean ocean water (V-SMOW). The analytical reproducibility for $\delta^{18}O$ in this study is ± 0.3 per mil.

5.3. Copper Isotopes

The copper isotope analysis was also conducted at ALS Minerals, and the procedure involves three main steps: sample digestion, target element isolation, and isotope ratio measurements. First, samples were prepared by closed vessel, MW-assisted sample digestion in HNO_3 + HCl + HF mixture (50 mg sample in 2 mL of acid mixture). Then, purify the digests using anion exchange chromatography following Marechal et al. (1999) [32] and Mason et al. (2005) [33], calibrate columns as per Borrok et al. (2007) [34], and collect at least 5 µg of Zn and 3 µg of Cu, possibly requiring two or three separations for >95% recovery. Next, the purified fractions with ICP-SFMS were analyzed to check concentrations and to remove interfering elements. The purified fractions were then evaporated to dryness and redissolved in 0.7 M HNO_3. Dilute the samples to 2000 ppb Zn and 500 ppb Cu, spike Zn solutions with Cu standard and Cu solutions with Zn standard for internal standards, and conduct isotope analyses with MC-ICP-MS (NEPTUNE PLUS, Thermo Fisher Scientific) in medium resolution mode. Delta values for Zn ($\delta^{68/64}Zn$) are calculated against IRMM-3702 CRM; delta values for $\delta^{65}Cu$ ($\delta^{65/63}Cu$) are calculated against NIST SRM 976; instrumental mass bias is corrected by isotopic ratios of Cu and Zn; standard deviation is calculated from two independent consequent measurements.

6. Results

6.1. Selected Mineral Chemistry

6.1.1. Feldspar

In matrices and phenocrysts of feldspar grains found in albitite, albite schist, and metagabbro, only ZK-303-22-Ab2 is identified as K-feldspar. In contrast, the others are predominantly pure albite (Ab_{97-99}, Tables 1 and S1, Figure 7). The content of other elements is low (<0.1%). These results are consistent with the widespread albitization observed in the region.

Table 1. Summary Statistics of Electron Probe Microanalysis (EPMA) feldspar data.

	Na₂O	V₂O₅	SiO₂	TiO₂	MgO	NiO	K₂O	Cr₂O₃	Al₂O₃	CaO	MnO	FeO	Total
						Albite (n = 60)							
mean	10.80	0.01	68.14	0.01	0.00	0.01	0.07	0.01	20.55	0.10	0.01	0.04	99.77
std	0.39	0.02	1.02	0.02	0.01	0.02	0.03	0.02	0.65	0.09	0.01	0.05	0.7
min	9.45	0.00	65.92	0.00	0.00	0.00	0.03	0.00	18.92	0.01	0.00	0.00	98.39
median	10.85	0.00	68.13	0.00	0.00	0.00	0.07	0.00	20.67	0.07	0.00	0.03	99.67
max	11.54	0.07	70.35	0.07	0.03	0.06	0.15	0.06	22.10	0.49	0.05	0.17	101.58
						K-feldspar (n = 1)							
303-22-Ab2	0.61	0.00	64.74	0.00	0.00	0.00	15.52	0.00	19.08	0.01	0.04	0.02	100.03

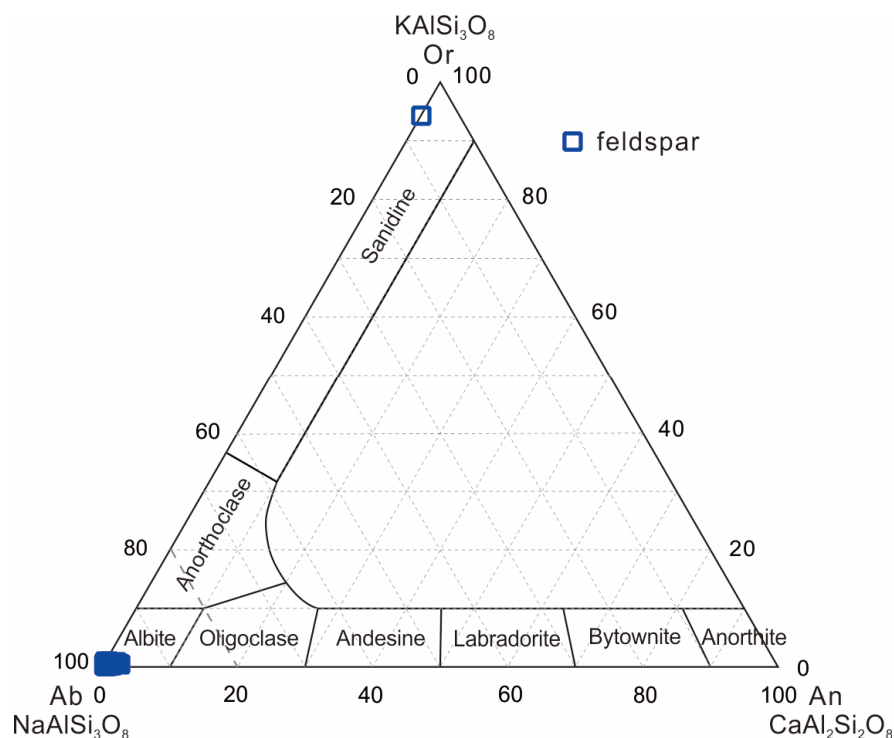Notes: All the concentrations in wt. %.

Figure 7. The feldspar compositional ternary diagram. Note that most of the samples are plotted in the field of albite.

6.1.2. Magnetite

Iron oxide makes up the majority of magnetite, with trace amounts of other elements (Tables 2 and S2). The content ranges for TiO_2 and V_2O_5 are 0.00 to 1.39% and 0.00 to 0.56%, respectively. SiO_2 and Al_2O_3 have average concentrations of 0.10 ± 0.15 and $0.16 \pm 0.19\%$, respectively. The average Na, Mg, Ni, K, Cr, Ca, and Mn concentrations are less than 0.10%.

The diagram by Dupuis and Beaudoin (2011) [35], contrasting Ni + Cr with Si + Mg, effectively differentiates magnetite associated with magmatic Ni-Cu deposits from those in other deposit types. Six samples were identified within the field of Ni-Cu deposits with relatively high Ni + Cr values (Figure 8A). In the Ca + Al + Mn versus Ti + V diagram from the same study, these six samples were excluded. Notably, in this diagram, the majority of magnetite is plotted within or near the IOCG field (Figure 8B).

Table 2. Summary Statistics of Electron Probe Microanalysis (EPMA) Magnetite Data.

	Na$_2$O	V$_2$O$_5$	SiO$_2$	TiO$_2$	MgO	NiO	K$_2$O	Cr$_2$O$_3$	Al$_2$O$_3$	CaO	MnO	FeO	Total
mean	0.02	0.20	0.10	0.10	0.01	0.04	0.01	0.05	0.16	0.02	0.01	94.64	95.35
std	0.02	0.15	0.15	0.24	0.01	0.04	0.01	0.05	0.19	0.02	0.02	1.17	0.89
min	0.00	0.00	0.00	0.00	0.00	0.00	0.00	0.00	0.01	0.00	0.00	91.50	92.49
mdian	0.01	0.16	0.05	0.05	0.01	0.03	0.00	0.04	0.10	0.02	0.00	94.86	95.48
max	0.10	0.56	0.75	1.39	0.05	0.15	0.03	0.21	0.95	0.11	0.07	96.30	96.58

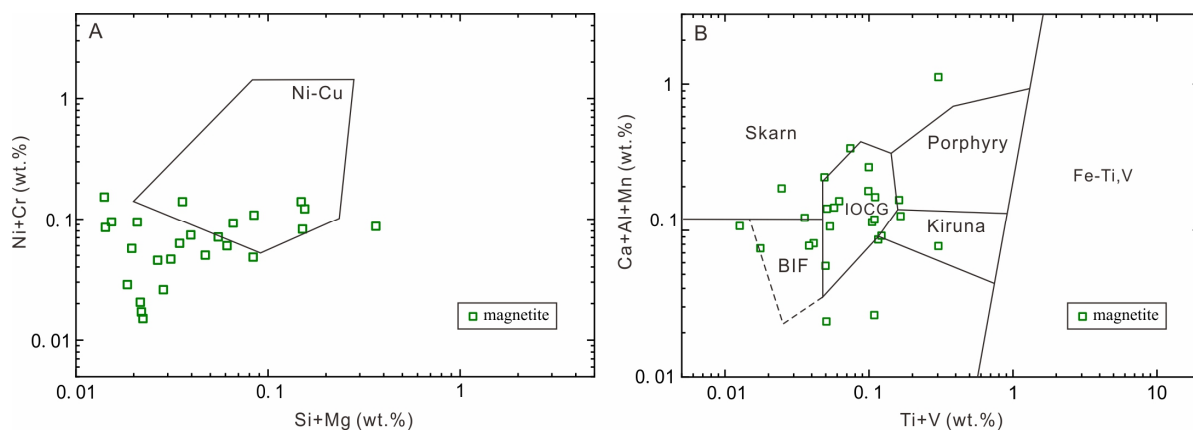Notes: All the concentrations in wt. %.

Figure 8. Magnetite discriminant diagram (after Dupuis and Beaudoin, 2011) [35]. (**A**) Ni + Cr vs. Si + Mg diagram for magnetite (*n* = 32). Note that six samples are plotted within the Ni-Cu region. (**B**) Ca + Al + Mn vs. Ti + V diagram for magnetite, with the six samples excluded from the Ni-Cu deposits field in Figure (**A**).

6.2. Estimation of Magnetite Formation Temperature

Magnetite formation temperature was estimated using the empirical geothermometer (T_{Mg-mag}, °C) developed by Canil and Lacourse (2020) [10], which is expressed as $T_{Mg-mag} = -8344\,(\pm 320)/[\ln X_{Mg}-4.1(\pm 0.28)]-273$. Data below the detection limit for Mg were excluded from the calculation. The majority of samples have temperatures within the range of 350 to 450 °C. Thus, 400 ± 50 °C was taken as the formation temperature of the magnetite. The magnetite stage is comparable to Stage II of the Lala deposit [1], which stage has fluid inclusion homogenization temperatures between 380 °C and 430 °C. Therefore, the temperature of 400 ± 50 °C is considered a reliable estimate for the formation temperature of magnetite. Furthermore, most samples were drawn within the intermediate-temperature hydrothermal range on the Al + Mn versus Ti + V diagram (Figure 9) [36].
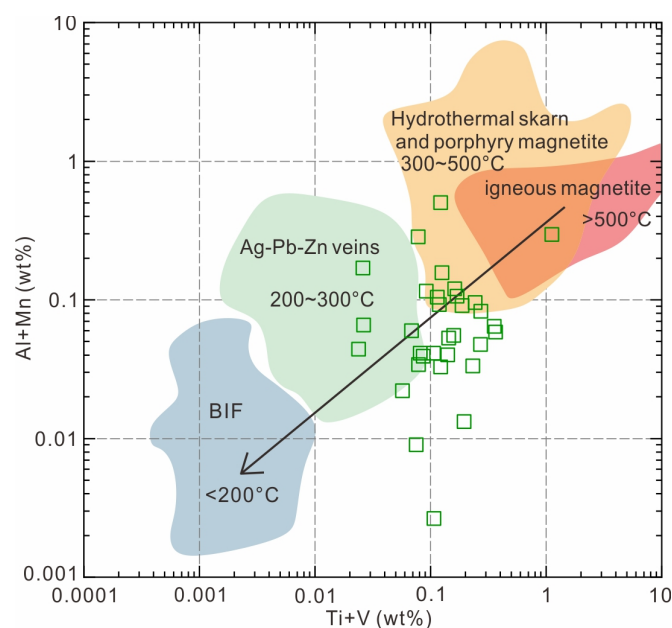

Figure 9. Ti + V vs. Al + Mn diagram of magnetite, used to identify the temperature range of magnetite formation (after Nadoll et al., 2014) [36]. Most of the samples are plotted within the medium-temperature range.

6.3. Stable Isotope Geochemistry

6.3.1. Oxygen Isotope Compositions of Magnetite

Magnetite from stage II has $\delta^{18}O$ values ranging from 1.4 to 4.1‰ ($n = 5$); on the basis of the temperature of 400°, the calculated $\delta^{18}O$ values of fluids vary from 8.3 to 11.0‰ ($n = 5$; Table 3).

Table 3. Oxygen Isotope Composition of Magnetite Associated with Hydrothermal Fluids from the Hongnipo Deposit.

Sample No.	Stage	Minerals	$\delta^{18}O$	Depth (m)	T (°C)	$\delta^{18}O_{fluid}$
ZK-301-24	III	magnetite	1.8	263.3	400 ± 50	8.7
ZK-301-25	III	magnetite	2.0	264.6	400 ± 50	8.9
ZK-302-5	III	magnetite	4.1	389.6	400 ± 50	11.0
ZK-303-3	III	magnetite	3.1	247.5	400 ± 50	10.0
ZK-303-35	III	magnetite	1.4	990.7	400 ± 50	8.3

Depth represents the distance along the corresponding borehole of the sample. Temperatures are estimated based on the calculation of trace elements of magnetite. Isotope fractionation equations for magnetite: $\delta^{18}O_{fluid} = \delta^{18}O_{magnetite} - (-3.7 - 1.47 \times 106/T^2)$.

6.3.2. Sulfur Isotope Compositions of Sulfides

The $\delta^{34}S_{VCDT}$ values of sulfide minerals exhibit two distinct categories (Table 4, Figure 10). Within different stratigraphic members, samples from the upper Luodang Formation predominantly display negative values, nearing zero ($\delta^{34}S_{VCDT} = -2.6$ to -0.1‰, $n = 3$). Conversely, sulfides originating from the lower Tianshengba Formation showcase a broader $\delta^{34}S_{VCDT}$ range, spanning from -3.0 to $+10.9$‰ ($n = 10$), with a predominant positive trend (Table 4). In the vertical direction, as the depth decreases, the range of $\delta^{34}S_{VCDT}$ values gradually widens (Figure 10B). There is no compelling difference between the $\delta^{34}S_{VCDT}$ values of sulfides from the banded sulfide stage (II) and the sulfide vein/stockwork stage (IV). Both stages have a relatively wide variation in the $\delta^{34}S_{VCDT}$ values, ranging from -2.6 to 10.9‰ ($n = 7$) and -1.5 to 9.9‰ ($n = 5$), respectively (Table 4). In samples ZK-301-16 and ZK-301-19, pyrite exhibits slightly higher $\delta^{34}S_{VCDT}$ values than the intergrown chalcopyrite. Similarly, in sample ZK-302-17, the $\delta^{34}S_{VCDT}$ value of pyrrhotite is higher than that of the intergrown chalcopyrite (Figure 10B). These data were integrated and compared with available data from the Lala deposit.

Table 4. Sulfur Isotope Composition of Sulfides from the Hongnipo Deposit.

Sample No.	Stage	Depth (m)	Stratum	Mineral	$\delta^{34}S$
ZK-305-9	II	258.2	LTSBF	Ccp	3.0
ZK-302-5	II	389.6	LTSBF	Py	5.5
ZK-301-15	II	450.6	LTSBF	Py	10.9
ZK-301-18	II	461.5	LTSBF	Ccp	0.8
ZK-301-19	II	472.9	LTSBF	Py	−0.7
	II	472.9	LTSBF	Ccp	−1.6
ZK-301-2	II	1002.5	ULDF	Po	−2.6
ZK-303-10	II/IV	406.5	LTSBF	Ccp	−3.0
ZK-308-2	IV	410	LTSBF	Ccp	9.9
ZK-301-16	IV	457	LTSBF	Ccp	6.5
	IV	457	LTSBF	Py	7.1
ZK-302-17	IV	808	ULDF	Ccp	−1.5
	IV	808	ULDF	Po	−0.1

Abbreviations: LTSBF = lower Tianshengba formation, ULDF = upper Luodang formation, Py = pyrite, Ccp = chalcopyrite, Po = pyrrhotite.
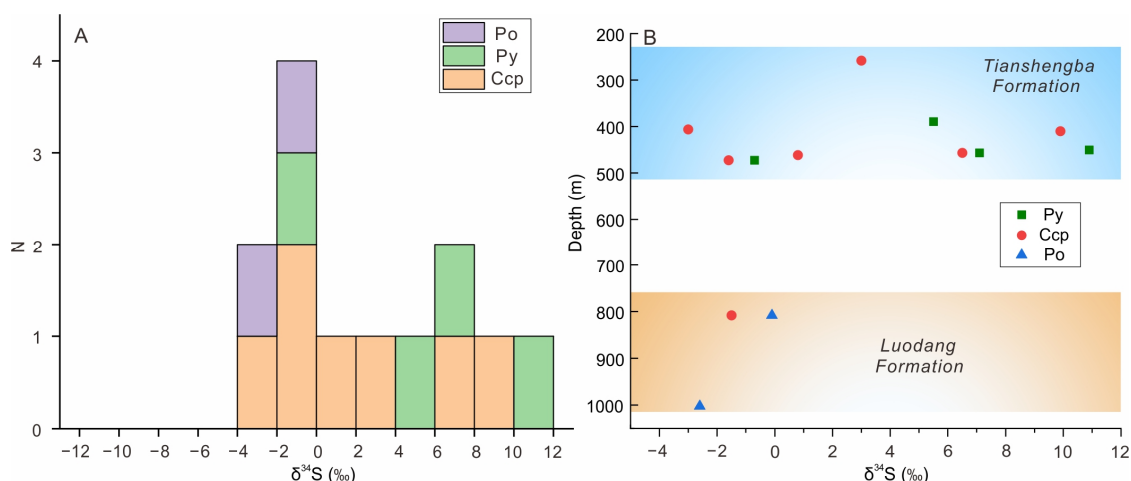
Figure 10. (**A**) Histogram showing $\delta^{34}S$ values of sulfides from Hongnipo deposit. (**B**) A distribution diagram of $\delta^{34}S$ values for sulfides at different depths.

6.3.3. Copper Isotope Compositions of Chalcopyrite

The $\delta^{65}Cu$ values for chalcopyrite from Hongnipo range between -0.135 ± 0.051 and $0.587 \pm 0.048‰$ (Table 5). Samples from Stage II have $\delta^{65}Cu$ values close to 0 ($-0.135‰$ and $0.071‰$), whereas those from Stage IV display higher values (ranging from $0.319‰$ to $0.587‰$). In Stage IV, the $\delta^{65}Cu$ values within the sulfide stockworks ($0.523‰$ and $0.587‰$) are higher than those in the sulfide vein ($0.319‰$). The mixed sample (ZK-30-3-10) has an intermediate $\delta^{65}Cu$ value ($0.240‰$).

Table 5. Copper Isotope Composition of Chalcopyrite from the Hongnipo Deposit.

Sample No.	Mineral	$\delta^{65}Cu$ (‰)	2SD (‰)	Ore Type	Stage
ZK-305-9	Ccp	−0.135	0.051	Laminated	II
ZK-301-19	Ccp	0.071	0.049	Laminated	II
ZK-303-10	Ccp	0.240	0.043	Laminated/vein	II/IV
ZK-301-16	Ccp	0.319	0.039	vein	IV
ZK-308 19-2	Ccp	0.523	0.048	stockwork	IV
ZK-302-17	Ccp	0.587	0.048	stockwork	IV
duplicated samples					
ZK-305-9	Ccp	-0.138	0.047		
ZK-301-16	Ccp	0.304	0.044		

Abbreviations: Ccp = chalcopyrite.

7. Discussion

7.1. Sodic Alteration in the Formation of the Hongnipo Deposit

The Hongnipo copper deposit is characterized by widespread sodic alteration. The occurrence of regional sodic alteration is a notable feature shared by both the deposits of the Kangdian region and other IOCG deposits worldwide (e.g., Lala Fe-Cu deposit; Yinachang Fe-Cu-(REE) deposit; Dahongshan Fe-Cu-(Au-Ag) deposit; Olympic Dam Cu-U-Au-Ag deposit; Ernest Henry Cu-Au deposit; Candelaria Cu-Au deposit; Salobo Cu-Au deposit) [1–3,37–40].

In the Lala Fe-Cu deposit, there is an extensive occurrence of albitite and albite–bearing schist, which Shentu (1986) [41] identified as the protolith represented by keratophyric rocks and siltite. The Hongnipo deposit has identical host rock types. Of the two, keratophyre is a leucocratic sodic intermediate albite–phyric volcanic rock [42], mainly composed of albite or orthoclase. Intermediate volcanic rocks often serve as host rocks for IOCG deposits. For instance, the Candelaria Cu-Au deposit, associated with andesitic and dacitic rock compositions [39]; the Ernest Henry Cu-Au deposit, with host rocks consisting of

plagioclase–phyric meta-andesitic rocks [38]; and the Mina Justa iron oxide-Cu (-Ag-Au) deposit, hosted within plagioclase–phyric andesite and andesitic volcaniclastic units [43]. Albite grains from the Hongnipo deposit exhibit rough surfaces and are often characterized by numerous inclusions, including fine-grained white mica and Fe-Ti oxides (Figure 5E,H,I). Engvik et al. (2008) [31] found that albite formed through sodic metasomatism is porous, and the development of these porosities, along with microfractures, ensures a large contact area between the reacting fluid and the parent minerals. Sodic alteration not only affects volcanic and sedimentary rocks but also impacts approximately contemporaneous gabbroic intrusions, where plagioclase has almost completely transformed into albite. Oliver et al. (2004) [44] concluded that during the process of sodic alteration, rocks underwent Na addition accompanied by the depletion of metallic elements such as Fe, Co, V, Mn, Pb, and Zn, as revealed through whole-rock geochemical analysis. In other words, sodic alteration might leach and extract metallic elements from the original rock. This finding may explain the strong correlation between sodic alteration and the formation of the Hongnipo deposit.

7.2. Origins of Magnetite and Associated Fluids

Despite being sporadically dispersed within the Hongnipo deposit, magnetite is a vital mineral because its chemical composition can be utilized to determine formation temperatures and distinguish between different deposit types [10,35]. The empirical geothermometer (T_{Mg-mag}, °C) suggests a magnetite formation temperature (stage III) of around 400 ± 50 °C. This aligns with the Ti + V versus Al + Mn diagram for magnetite, indicating its moderate temperature characteristic (Figure 9). In the Ni + Cr versus Si + Mg diagram, some magnetite grains are situated within the spectrum of magmatic Ni-Cu deposits (Figure 8A) [35]. Despite the absence of gabbroic rocks in the host units, this placement indicates a close connection with mafic magmatic rocks. Furthermore, a significant portion of magnetite is plotted within the IOCG deposits field (Figure 8B), suggesting a shared origin between the magnetite in the Hongnipo and other IOCG deposits. The calculated $\delta^{18}O$ values of fluids in equilibrium with magnetite range from 8.3 to 11.0‰ (Table 3). This range overlaps with the magnetite stages in deposits such as Ernest Henry, Olympic Dam, Osborne, and Mount Elliott in Australia, as well as with Stage II (magnetite stage) and Stage III (magnetite–polymetallic sulfide stage) of the Lala deposit (Figure 11), all indicating magmatic water origins [1,45,46]. Hence, we suggest that the magnetite in the Hongnipo deposit has a primordial magmatic origin.
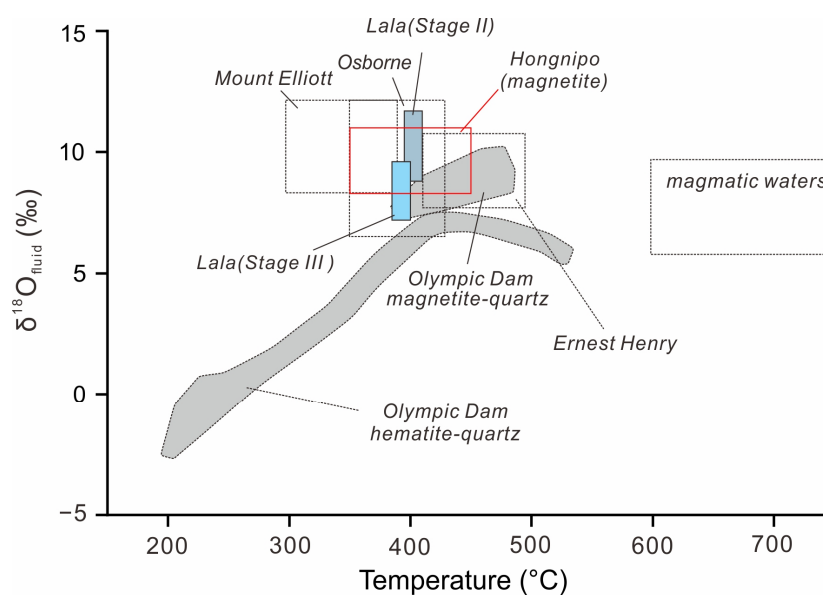

Figure 11. $\delta^{18}O$ fluid-temperature diagram of the Hognnipo deposit and other IOCG deposits in the world. Data were obtained from Williams et al. (2005) [46] and Chen and Zhou (2012) [1].

7.3. Sulfur and Copper Sources

The Luodang Formation in the Hongnipo copper deposit occurs at greater depths and exhibits sulfur isotope values close to zero (Figure 10B), consistent with the typical range for magmatic sulfur. Additionally, this formation contains abundant volcanic rocks and sporadically distributed gabbroic intrusions, all indicating a significant contribution of magmatic-sourced sulfur. In contrast, sulfur isotope values in the Tianshengba Formation are mainly positive and show considerable variation (Figure 10B). Given that the underlying Luodang Formation is primarily composed of magmatic sulfur, it is difficult to attribute such a wide range of values to a single sulfur source. The high positive values, reaching up to 10.9‰, likely indicate a contribution from reduced seawater sulfate, as such values are consistent with sulfate reduction under diagenetic conditions, where thermochemical processes convert sulfate to H_2S with an enriched $\delta^{34}S$ signature. The range observed in the Tianshengba Formation (-3.0 to 10.9‰) aligns with the model proposed by Ohmoto and Goldhaber (1997) [47], suggesting a mixing of magmatic H_2S and reduced seawater sulfate.

There is no statistically significant difference in the sulfur isotope values between the two stages of mineralization: the banded sulfide stage (II) ranges from -2.6 to 10.9‰, and the sulfide vein/stockwork stage (IV) ranges from -1.5 to 9.9‰. Lin et al. (2020) [6] performed an in situ investigation of sulfur isotopes on 25 points from 9 samples at Hongnipo, showing that sulfide minerals from the sulfide vein stage consistently had lower $\delta^{34}S$ values than those from the banded sulfide stage. Similar results were reported by Song et al. (2023) [9] based on 11 points from 3 samples, indicating a similar trend of lower $\delta^{34}S$ values in the later sulfide vein stage. While these trends suggest some degree of differentiation, the conclusions are limited by small sample sizes in all studies, including our own, highlighting the need for more extensive datasets to achieve more reliable insights into sulfur isotope distribution across different mineralization stages.

Chalcopyrite formation in hydrothermal deposits primarily occurs through two mechanisms. The first mechanism involves direct nucleation from hydrothermal fluids, as evidenced by the presence of dendritic chalcopyrite crystals in some submarine hydrothermal chimneys. The second, more common mechanism is the replacement of preexisting sulfide minerals, such as pyrite, pyrrhotite, sphalerite, and galena [47,48]. This replacement can occur in two distinct forms: one involving only solid-phase sulfide sulfur, resulting in $\delta^{34}S$ values of chalcopyrite that are consistent with those of the precursor minerals, and another involving H_2S in hydrothermal fluids, where the $\delta^{34}S$ values of chalcopyrite differ from those of the host sulfides. In the Hongnipo deposit, dendritic chalcopyrite crystals have not been identified; however, chalcopyrite filling and replacing pyrite and pyrrhotite are widely observed (Figure 5D). Chalcopyrite typically exhibits lower $\delta^{34}S$ values compared to coexisting pyrite and pyrrhotite. We thus speculate that the primary mechanism by which chalcopyrite is created is the substitution of the original sulfides (pyrite/pyrrhotite), which occurs when hydrothermal fluids containing H_2S with $\delta^{34}S$ values lower than those of the host sulfides are involved.

The abundant sulfur isotope data from earlier studies of the Lala deposit were compared with the available data from the Hongnipo deposit (Figure 12, Table S3). An overall characteristic emerges without distinguishing between mineralization stages: Both deposits exhibit a wide range of $\delta^{34}S$ values, displaying approximately normal distributions. Notably, the Lala deposit has a more tightly clustered distribution of $\delta^{34}S$ values with a slight variance, primarily concentrated within the 0 to 4‰ range (>75% of values). In contrast, the Hongnipo deposit presents a more dispersed distribution of $\delta^{34}S$ values, with a higher prevalence of samples featuring positive $\delta^{34}S$ values. The Lala deposit is located within the Luodang Formation and at a deeper stratigraphic level than the majority of the Hongnipo deposit (i.e., Tianshengba Formation). The transition in sulfur isotope distribution from the Lala to Hongnipo deposit suggests a shift from predominantly magmatic-derived sulfur to a mixing of magmatic and non-magmatic sulfur (Figure 13). This observation suggests that the Lala deposit is situated in a vertical orientation near a deep-seated magma chamber, which aligns with the pattern found in the Olympic Dam deposit [49]. The Hongnipo

deposit, on the other hand, is situated nearer the paleosurface and farther from the magma chamber. Consequently, it is produced by adding a higher amount of non-magmatic sulfur.

Many studies have shown that copper minerals precipitated from high-temperature fluids show low fractionation [50–53]. The new δ^{65}Cu data reported here, which have a narrow range from -0.135 to 0.587‰, suggest that both stages of copper mineralization of the Hongnipo occurred at high temperatures, which is consistent with the fluid inclusion results [9]. The range of the finding is comparable to primary Cu-sulfides in most hydrothermal deposits and even in magmatic Ni-Cu sulfide deposits (Figure 14A). Because the variation generated by redox processes inside a deposit is typically larger than that caused by inter-deposit factors, it is challenging to distinguish between different deposit types or Cu sources using a limited amount of Cu isotope data [54].

The δ^{65}Cu values for stage II chalcopyrite, -0.135 and 0.071‰, are close to the bulk silicate Earth δ^{65}Cu average (0.06 ± 0.20 [2SD]) [55]. Chalcopyrite from Stage IV has higher δ^{65}Cu values, suggesting that this stage of copper mineralization may have precipitated from different sources from that of Stage II or that copper isotope ratios of Stage IV have undergone some degree of fractionation based on activation of Stage II copper minerals, e.g., fluid–rock reaction, fluid mixing. The qualitative correlation between the Cu isotope values of the Hongnipo and the ore grade might be attributed to the greater amounts of heavy Cu that tended to integrate into the chalcopyrite crystals during the process of evolution. On the other hand, the copper isotope value of the mixed sample may represent a mixing of two stages of copper isotope ratios. Still, the database is much too limited to draw significant conclusions.
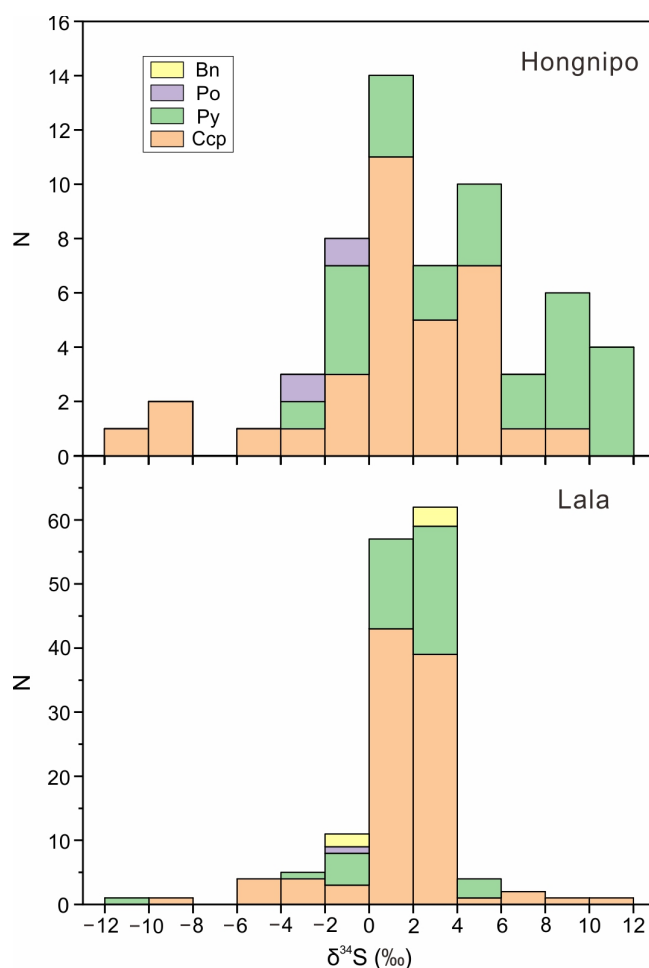

Figure 12. Histogram showing general δ^{34}S values of sulfides from the Hongnipo and Lala deposits. The data for the Hongnipo deposit are from Zhang (2019) [56], Lin et al. (2020) [6], Song et al. (2023) [9],

and this study, while the data for the Lala deposit are from Chen and Ran (1992) [57], Shentu (1997) [58], He (2009) [59], Zhu (2011) [60], and Chen and Zhou (2012) [1]. Notably, an extremum of $-28.6‰$ is included in the range of -12 to $-10‰$.
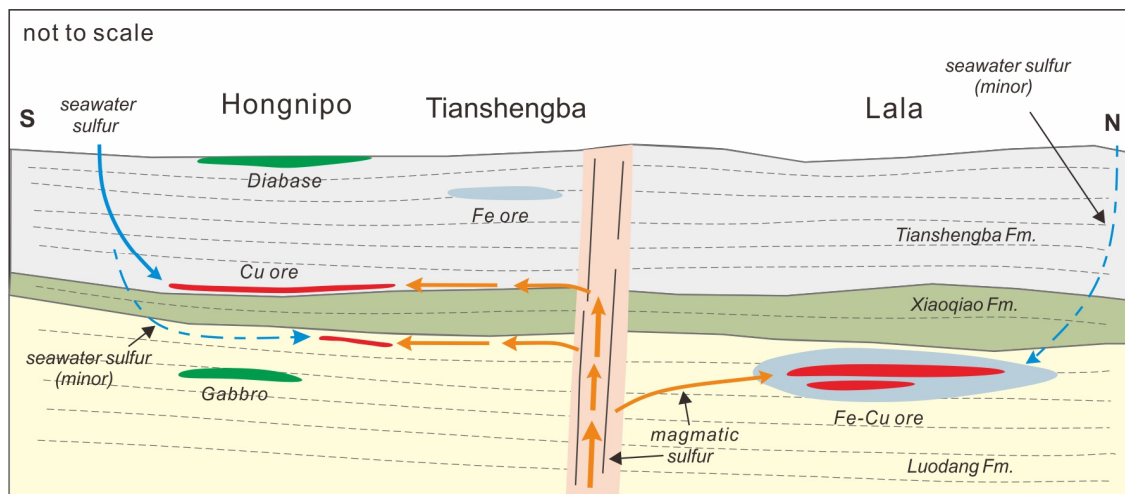

Figure 13. Schematic diagram illustrating the difference in the sources of sulfur between the Hongnipo and Lala deposits. The dashed lines in the strata represent foliation.

There is no systematic correlation between $\delta^{65}Cu$ and $\delta^{34}S$ values from the same sample (Figure 14B, Table S4), which may be attributed to the fact that copper and sulfur have different geochemical behaviors during mineralization. At high temperatures, sulfur has two distinct species: SO_2 and H_2S. There is a considerable equilibrium isotopic fractionation between the two. In contrast, significant isotopic fractionation between Cu species only happens in oxidized low-temperature hydrothermal fluids, while Cu has just one major species in high-temperature hydrothermal solutions. Li et al. (2010) also found no consistent correlation between the $\delta^{65}Cu$ and $\delta^{34}S$ data from the Northparkes porphyry Cu-Au deposit [61].
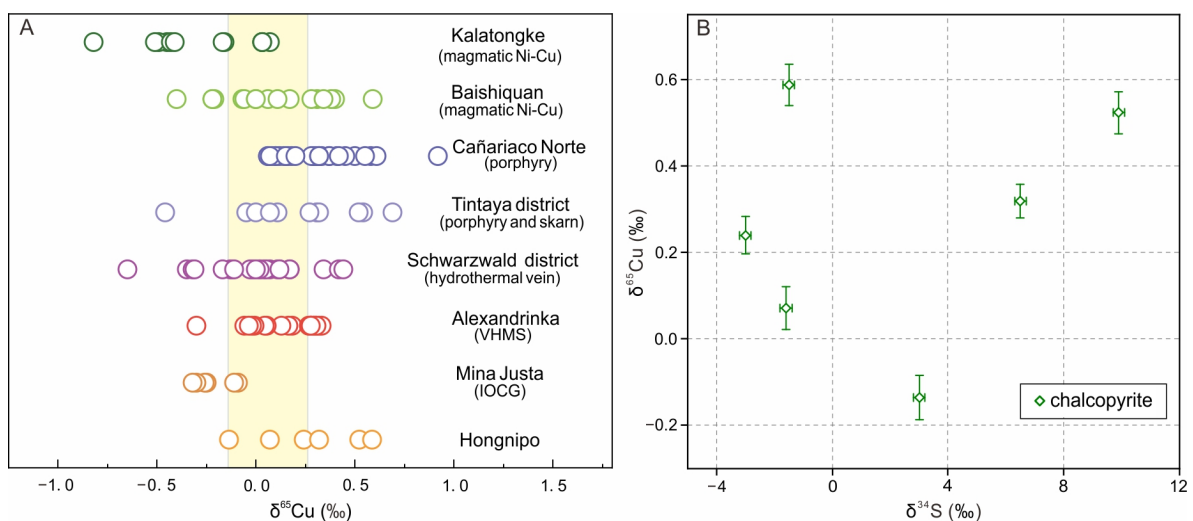

Figure 14. (**A**) Copper isotope compositions of various copper deposits from several different types. The yellow area represents the bulk silicate Earth $\delta^{65}Cu$ average (0.06 ± 0.20 [2SD]). Data for other deposits are from Larson et al., 2003 [62], Mason et al., 2005 [33], Markl et al., 2006 [54], Mathur et al., 2012 [63], Tang et al., 2020 [64], and Rodriguez-Mustafa et al., 2022 [65]. (**B**) The plot of $\delta^{65}Cu$ versus $\delta^{34}S$ values for chalcopyrite samples from the Hongnipo deposit.

7.4. Classification of the Hongnipo Copper Deposit

The Hongnipo deposit's early layered mineralization was characterized as a VMS-type mineralization due to its mixed sulfur sources, rifting setting, and ore structures [6]. However, the deposits have a close affinity for Cu with Ag, Co, As, and Sb but lack Zn, comparable to major IOCG deposits elsewhere in the world [46,66].

In the classification by Groves et al. (2010) [28], Iron Oxide–Copper–Gold (IOCG) sensu stricto deposits are (1) magmatic–hydrothermal deposits that contain economic Cu and Au, (2) structurally controlled and typically contain abundant breccia, (3) associated with regional-scale sodic or sodic–calcic alteration, predating the sulfide precipitation, (4) closely related to abundant low Ti iron oxides and/or iron silicates, which are often present earlier than the Cu mineralization, (5) characterized by LREE enrichment and low S sulfide (lack of abundant pyrite) and lack widely distributed quartz veins or silicification, (6) closely linked in time with major magmatic intrusions but not necessarily in close spatial proximity.

Based on O, S, and Cu isotope studies, the Hongnipo deposit has a primarily magmatic–hydrothermal origin but only contains economic Cu without subordinate Au. The host rocks of the ores are metamorphic volcanic and sedimentary rocks. Extensive hydrothermal alteration is identified and characterized predominantly by albitization, mica alteration, carbonatization, and chlorination. The orebodies are strata-bound, and their deformation occurs synchronously with the folding of the strata. Metamorphism has been a significant factor in the process. The early banded sulfides were formed through metasomatism of hydrothermal fluids along the foliation, while the distribution of later sulfide veins was also influenced by the metamorphism. Breccia is only locally distributed within the deposit. Sodic alteration is widely distributed in the Hongnipo deposit and throughout the entire region (Figure 7) [1].

The average content of Fe in the host rocks and ores is approximately 10–14% [8]. Combined hand specimen and microscopic analysis, iron mainly occurs in the form of Fe-Ti oxides, iron silicates (e.g., biotite, hornblende, and chlorite), and iron-bearing carbonate minerals (e.g., siderite and ankerite). Fe-Ti oxides are primarily composed of magnetite and ilmenite, with subordinate amounts of titanomagnetite and rutile. Low-Ti iron oxides include magnetite and hematite, which primarily occur as disseminated aggregates and veins, respectively. The Hongnipo deposit is surrounded by several iron occurrences, namely Tianshengba, Guandi, and Lijiafen (Figure 1C), where magnetite is the predominant ore mineral.

Copper and iron were generated through separate mineralization processes (stage II, IV, and stage III), simultaneously resulting in spatial separation in the district. There are some similarities between this pattern and the Dahongshan deposit [4,67], which has different types of Fe and Cu-Fe orebodies in different parts of the deposit. Williams et al. (2005) [46] suggested that the formation of ironstones might not be connected to the processes that deposit Cu-Au and that the distribution of Cu-Au can be partly separate from ironstone at the district to mine level. This investigation yielded similar results. The contents of LREEs are not yet available. Chalcopyrite, the principal ore mineral, is frequently found intergrown with pyrite during the two stages of Cu mineralization (Figure 6). In some cases, pyrite concentration surpasses chalcopyrite content, especially in the ore generated during the banded sulfide stage (Figures 4E and 5D). Quartz veins and silicification are subordinate, while albite, mica, and carbonate constitute the main gangue minerals. The gabbroic intrusions within the deposit are sparsely distributed and closely associated with nearly contemporaneous volcanic rocks (Figures 1C and 2B; ~1.7 Ga) [26].

The Kangdian region contains numerous Fe-Cu deposits with ore textures, mineralogy, alteration assemblages, and multi-stage mineralization typical of IOCG-type deposits, making it defined as an IOCG metallogenic province [2,27,67,68]. The Lala Fe-Cu deposit, located approximately 5 km north of the Hongnipo deposit (Figure 1C), is considered a typical IOCG deposit due to its significant association of Fe and Cu, as well as the enrichment of Au and LREEs [1,26]. Although the Hongnipo deposit shares numerous characteristics with Lala and other representative IOCG deposits worldwide, it also displays

particular distinctions: these include a notable absence of significant enrichment in low-Ti Fe oxides and Au, alongside abundant pyrite. Overall, this study tends to classify the Hongnipo copper deposit as a Cu-rich section in a typical IOCG deposit [46].

8. Conclusions

The Hongnipo copper deposit, a newly discovered large deposit in the Kangdian metallogenic belt, contains abundant chalcopyrite with sparsely distributed magnetite. The deposit is associated with pervasive pre-ore sodic alteration, and the magnetite exhibits characteristics of a magmatic origin. During chalcopyrite formation, S and Cu display distinct geochemical behaviors, with sulfur derived from a mixture of magmatic H_2S and reduced seawater sulfur, while copper precipitates from a high-temperature, relatively homogeneous source.

The close association of Cu with Ag, Co, As, and Sb, along with the alteration of mineral assemblages and stratigraphic control, are comparable to other IOCG deposits worldwide. However, due to the scarcity of significant low-Ti iron oxides and gold and its setting amidst several Fe occurrences, we classify the Hongnipo deposit as a copper-rich section within a typical IOCG deposit.

Supplementary Materials: The following supporting information can be downloaded at: https://www.mdpi.com/article/10.3390/min14090936/s1, Table S1: Results of Electron Probe Microanalysis (EPMA) Feldspar Data; Table S2: Results of Electron Probe Microanalysis (EPMA) Magnetite Data; Table S3: Sulfur Isotope Composition of Sulfides from the Hongnipo and Lala Deposits; Table S4: Copper Isotope Composition of Primary Sulfide from Various Deposits.

Author Contributions: Conceptualization, W.Y. and G.W.; investigation, W.Y.; methodology, Y.X.; visualization, W.Y.; writing—original draft preparation, W.Y.; writing—review and editing, G.W.; project administration, G.W. All authors have read and agreed to the published version of the manuscript.

Data Availability Statement: All of the data used in this article are included in the Supplementary Materials.

Conflicts of Interest: The authors declare no conflicts of interest.

References

1. Chen, W.T.; Zhou, M.F. Paragenesis, Stable Isotopes, and Molybdenite Re-Os Isotope Age of the Lala Iron-Copper Deposit, Southwest China. *Econ. Geol.* **2012**, *107*, 459–480. [CrossRef]
2. Zhou, M.F.; Zhao, X.F.; Chen, W.T.; Li, X.C.; Wang, W.; Yan, D.P.; Qiu, H.N. Proterozoic Fe–Cu Metallogeny and Supercontinental Cycles of the Southwestern Yangtze Block, Southern China and Northern Vietnam. *Earth Sci. Rev.* **2014**, *139*, 59–82. [CrossRef]
3. Li, X.; Zhao, X.; Zhou, M.F.; Chen, W.T.; Chu, Z. Fluid Inclusion and Isotopic Constraints on the Origin of the Paleoproterozoic Yinachang Fe-Cu-(REE) Deposit, Southwest China. *Econ. Geol.* **2015**, *110*, 1339–1369. [CrossRef]
4. Zhao, X.F.; Zhou, M.F.; Su, Z.K.; Li, X.C.; Chen, W.T.; Li, J.W. Geology, Geochronology, and Geochemistry of the Dahongshan Fe-Cu-(Au-Ag) Deposit, Southwest China: Implications for the Formation of Iron Oxide Copper-Gold Deposits in Intracratonic Rift Settings. *Econ. Geol.* **2017**, *112*, 603–628. [CrossRef]
5. Gong, L.M.; Shen, H.M.; Huang, S.Z.; Wang, Y.; Zou, F.; Xiao, Y.C.; Li, Y.; Zhang, X.Y.; Zhang, C.; Li, G.Q.; et al. *The Report of Copper Exploration of Hongnipo Ore District, Huili County, Sichuan Province*; Geological Team 403 of Sichuan Geological and Mineral Exploration and Development Bureau: Leshan, China, 2016. (In Chinese)
6. Lin, L.; Chen, R.; Pang, Z.; Chen, H.; Xue, J.; Jia, H. Sulfide Rb—Sr, Re—Os and In Situ S Isotopic Constraints on Two Mineralization Events at the Large Hongnipo Cu Deposit, SW China. *Minerals* **2020**, *10*, 414. [CrossRef]

7. Yang, W.D.; Gao, F.L.; Wang, G.W.; Pang, Z.S.; Shen, H.M.; Gong, L.M.; Shen, H.T.; Zhang, Z.Q.; Liu, X.N. 3D Geological Modeling and New Understanding of Ore-controlling Tectonic Evolution of the Hongnipo Copper Deposit in Sichuan Province. *Geoscience* **2020**, *34*, 598–608. (In Chinese with English Abstract)

8. Lin, C.G.; Cheng, Z.Z.; Chen, H.; Lv, Z.C.; Pang, Z.S.; Chen, X.; Shen, H.M. Primary halo characteristics and prospecting direction of Hongnipo copper deposit, Sichuan Province. *Geol. China* **2023**, *50*, 837–852, (In Chinese with English Abstract).

9. Song, M.W.; Peng, Y.W.; Chen, C.H.; Ding, F.; Cheng, W.B.; Li, B.H.; Yang, Y.L.; Chen, L.; Wu, J.; Chen, X. Ore-forming fluid characteristics and copper mineralization mechanism in the Hongnipo copper deposit, southwestern margin of Yangtze Block: Evidence from in-situ S isotopes and fluid inclusions. *Acta Petrol. Mineral.* **2023**, *42*, 629–651, (In Chinese with English Abstract).

10. Canil, D.; Lacourse, T. Geothermometry Using Minor and Trace Elements in Igneous and Hydrothermal Magnetite. *Chem. Geol.* **2020**, *541*, 119576. [CrossRef]

11. Li, Z.X.; Zhang, L.; Powell, C. McA. South China in Rodinia: Part of the Missing Link between Australia–East Antarctica and Laurentia? *Geology* **1995**, *23*, 407–410. [CrossRef]

12. Li, Z.X.; Li, X.; Zhou, H.; Kinny, P.D. Grenvillian Continental Collision in South China: New SHRIMP U-Pb Zircon Results and Implications for the Configuration of Rodinia. *Geology* **2002**, *30*, 163–166. [CrossRef]

13. Wang, X.L.; Zhou, J.C.; Griffin, W.L.; Wang, R.C.; Qiu, J.S.; O'Reilly, S.Y.; Xu, X.; Liu, X.M.; Zhang, G.L. Detrital Zircon Geochronology of Precambrian Basement Sequences in the Jiangnan Orogen: Dating the Assembly of the Yangtze and Cathaysia Blocks. *Precambrian Res.* **2007**, *159*, 117–131. [CrossRef]

14. Qiu, Y.M.; Gao, S.; McNaughton, N.J.; Groves, D.I.; Li, W.L. First Evidence of >3.2 Ga Continental Crust in the Yangtze Craton of South China and Its Implications for Archean Crustal Evolution and Phanerozoic Tectonics. *Geology* **2000**, *28*, 11–14. [CrossRef]

15. Li, X.; Li, Z.X.; Zhou, H.; Liu, Y.; Kinny, P.D. U–Pb Zircon Geochronology, Geochemistry and Nd Isotopic Study of Neoproterozoic Bimodal Volcanic Rocks in the Kangdian Rift of South China: Implications for the Initial Rifting of Rodinia. *Precambrian Res.* **2002**, *113*, 135–154. [CrossRef]

16. Li, H.; Zhang, Z.; Santosh, M.; Li, Y.; Han, L.; Zhu, J.; Pan, R. Geochronological, Geochemical and Sr–Nd Isotopic Fingerprinting of Neoproterozoic Mafic Dykes in the Western Margin of the Yangtze Block, SW China: Implications for Rodinia Supercontinent Breakup. *Precambrian Res.* **2019**, *331*, 105371. [CrossRef]

17. Ran, C.Y.; Liu, W.G. *Geochemistry of Copper Deposits and Their Mechanism of Storeyed Texture in Kangdian Axis*, 1st ed.; Science Press: Beijing, China, 1993; pp. 9–18, (In Chinese with Englilsh Abstract).

18. Zhao, X.F.; Zhou, M.F.; Li, J.W.; Sun, M.; Gao, J.F.; Sun, W.H.; Yang, J.H. Late Paleoproterozoic to Early Mesoproterozoic Dongchuan Group in Yunnan, SW China: Implications for Tectonic Evolution of the Yangtze Block. *Precambrian Res.* **2010**, *182*, 57–69. [CrossRef]

19. Fan, H.P.; Zhu, W.G.; Li, Z.X. Paleo- to Mesoproterozoic Magmatic and Tectonic Evolution of the Southwestern Yangtze Block, South China: New Constraints from ca. 1.7–1.5 Ga Mafic Rocks in the Huili-Dongchuan Area. *Gondwana Res.* **2020**, *87*, 248–262. [CrossRef]

20. Yang, Y.X.; Qiu, D.M.; Que, G.Y.; Zhang, L.S.; Wan, J. *Precambrian Stratabound Copper Deposits in Xichang-Central Yunnan Region*, 1st ed.; Chongqing Publishing House: Chongqing, China, 1988; pp. 8–12. (In Chinese with English Abstract)

21. Wu, M.D.; Duan, J.S.; Song, X.L.; Chen, L.; Dan, Y. *Geology of Kunyang Group in Yunnan Province*, 1st ed.; Scientific Press of Yunnan Province: Kunming, China, 1990; pp. 265–266. (In Chinese with English Abstract)

22. Sun, Z.M.; Yin, F.G.; Guan, J.L.; Liu, J.H.; Li, J.M.; Geng, Y.R.; Wang, L.Q. SHRIMP U–Pb dating and its stratigraphic significance of tuff zircons from Heishan Formation of Kunyang Group, Dongchuan area, Yunnan Province, China. *Geol. Bull. China* **2009**, *28*, 896–900. (In Chinese with English Abstract)

23. Greentree, M.R.; Li, Z.X.; Li, X.H.; Wu, H. Late Mesoproterozoic to Earliest Neoproterozoic Basin Record of the Sibao Orogenesis in Western South China and Relationship to the Assembly of Rodinia. *Precambrian Res.* **2006**, *151*, 79–100. [CrossRef]

24. Zhu, W.G.; Zhong, H.; Li, Z.X.; Bai, Z.J.; Yang, Y.J. SIMS Zircon U–Pb Ages, Geochemistry and Nd–Hf Isotopes of ca. 1.0Ga Mafic Dykes and Volcanic Rocks in the Huili Area, SW China: Origin and Tectonic Significance. *Precambrian Res.* **2016**, *273*, 67–89. [CrossRef]

25. Chen, W.T.; Sun, W.H.; Wang, W.; Zhao, J.H.; Zhou, M.F. "Grenvillian" Intra-Plate Mafic Magmatism in the Southwestern Yangtze Block, SW China. *Precambrian Res.* **2014**, *242*, 138–153. [CrossRef]

26. Zhu, Z.M.; Sun, Y.L. Direct Re—Os Dating Of Chalcopyrite from the Lala Iocg Deposit in the Kangdian Copper Belt, China. *Econ. Geol.* **2013**, *108*, 871–882. [CrossRef]

27. Zhao, X.F.; Zhou, M.F. Fe—Cu Deposits in the Kangdian Region, SW China: A Proterozoic IOCG (Iron-Oxide–Copper–Gold) Metallogenic Province. *Miner. Deposita* **2011**, *46*, 731–747. [CrossRef]

28. Groves, D.I.; Bierlein, F.P.; Meinert, L.D.; Hitzman, M.W. Iron Oxide Copper-Gold (IOCG) Deposits through Earth History: Implications for Origin, Lithospheric Setting, and Distinction from Other Epigenetic Iron Oxide Deposits. *Econ. Geol.* **2010**, *105*, 641–654. [CrossRef]

29. Zhu, Z.; Tan, H.; Liu, Y. Late Palaeoproterozoic Hekou Group in Sichuan, Southwest China: Geochronological Framework and Tectonic Implications. *Int. Geol. Rev.* **2018**, *60*, 305–318. [CrossRef]

30. Best, M.G. *Igneous and Metamorphic Petrology*, 2nd ed.; Blackwell Publishing: Malden, MA, USA, 2003; pp. 404–472.

31. Engvik, A.K.; Putnis, A.; Fitz Gerald, J.D.; Austrheim, H. Albitization of Granitic Rocks: The Mechanism of Replacement of Oligoclase by Albite. *Can. Mineral.* **2008**, *46*, 1401–1415. [CrossRef]

32. Maréchal, C.N.; Télouk, P.; Albarède, F. Precise Analysis of Copper and Zinc Isotopic Compositions by Plasma-Source Mass Spectrometry. *Chem. Geol.* **1999**, *156*, 251–273. [CrossRef]

33. Mason, T.F.D.; Weiss, D.J.; Chapman, J.B.; Wilkinson, J.J.; Tessalina, S.G.; Spiro, B.; Horstwood, M.S.A.; Spratt, J.; Coles, B.J. Zn and Cu Isotopic Variability in the Alexandrinka Volcanic-Hosted Massive Sulphide (VHMS) Ore Deposit, Urals, Russia. *Chem. Geol.* **2005**, *221*, 170–187. [CrossRef]

34. Borrok, D.M.; Wanty, R.B.; Ridley, W.I.; Wolf, R.; Lamothe, P.J.; Adams, M. Separation of Copper, Iron, and Zinc from Complex Aqueous Solutions for Isotopic Measurement. *Chem. Geol.* **2007**, *242*, 400–414. [CrossRef]

35. Dupuis, C.; Beaudoin, G. Discriminant Diagrams for Iron Oxide Trace Element Fingerprinting of Mineral Deposit Types. *Miner. Depos.* **2011**, *46*, 319–335. [CrossRef]

36. Nadoll, P.; Angerer, T.; Mauk, J.L.; French, D.; Walshe, J. The Chemistry of Hydrothermal Magnetite: A Review. *Ore Geol. Rev.* **2014**, *61*, 1–32. [CrossRef]

37. Oreskes, N.; Einaudi, M.T. Origin of Rare Earth Element-Enriched Hematite Breccias at the Olympic Dam Cu-U-Au-Ag Deposit, Roxby Downs, South Australia. *Econ. Geol.* **1990**, *85*, 1–28. [CrossRef]

38. Mark, G.; Oliver, N.H.S.; Williams, P.J. Mineralogical and Chemical Evolution of the Ernest Henry Fe Oxide–Cu–Au Ore System, Cloncurry District, Northwest Queensland, Australia. *Miner. Depos.* **2006**, *40*, 769–801. [CrossRef]

39. Marschik, R. The Candelaria-Punta Del Cobre Iron Oxide Cu-Au(-Zn-Ag) Deposits, Chile. *Econ. Geol.* **2001**, *96*, 1799–1826.

40. Requia, K.; Stein, H.; Fontbote, L.; Chiaradia, M. Re-Os and Pb-Pb Geochronology of the Archean Salobo Iron Oxide Copper-Gold Deposit, Carajas Mineral Province, Northern Brazil. *Miner. Depos.* **2003**, *38*, 727–738. [CrossRef]

41. Shentu, B.Y.; Liu, Z.N. Characteristics of the ore bearing rock series and the origin of the deposit, Lala copper mine western Sichuan. *Miner. Rocks* **1986**, *6*, 111–121. (In Chinese with English Abstract)

42. Schermerhorn, L.J.G. What Is Keratophyre? *Lithos* **1973**, *6*, 1–11. [CrossRef]

43. Chen, H.; Kyser, T.K.; Clark, A.H. Contrasting Fluids and Reservoirs in the Contiguous Marcona and Mina Justa Iron Oxide–Cu (–Ag–Au) Deposits, South-Central Perú. *Miner. Depos.* **2011**, *46*, 677–706. [CrossRef]

44. Oliver, N.H.S.; Cleverley, J.S.; Mark, G.; Pollard, P.J.; Fu, B.; Marshall, L.J.; Rubenach, M.J.; Williams, P.J.; Baker, T. Modeling the Role of Sodic Alteration in the Genesis of Iron Oxide-Copper-Gold Deposits, Eastern Mount Isa Block, Australia. *Econ. Geol.* **2004**, *99*, 1145–1176. [CrossRef]

45. Taylor, H.P. Oxygen and hydrogen isotope relationship in hydrothermal mineral deposits. In *Geochemistry of Hydrothermal Ore Deposits*, 3rd ed.; Barnes, H.L., Ed.; EWiley: New York, NY, USA, 1997; Volume 6, pp. 229–302.

46. Williams, P.J.; Barton, M.D.; Johnson, D.A.; Fontboté, L.; de Haller, A.; Mark, G.; Oliver, N.H.S.; Marschik, R. Iron Oxide Copper-Gold Deposits: Geology, Space-Time Distribution, and Possible Modes of Origin. In *One Hundredth Anniversary Volume*; Society of Economic Geologists: Littleton, CO, USA, 2005; ISBN 978-1-887483-01-8.

47. Ohmoto, H.; Goldhaber, M.B. Sulfur and Carbon Isotopes. In *Geochemistry of Hydrothermal ore Deposits*, 3rd ed.; Barnes, H.L., Ed.; Wiley: New York, NY, USA, 1997; Volume 11, pp. 229–302.

48. Eldridge, C.S.; Barton, P.B.; Ohmoto, H. Mineral Textures and Their Bearing on Formation of the Kuroko Orebodies. In *The Kuroko and Related Volcanogenic Massive Sulfide Deposits*; Society of Economic Geologists: Littleton, CO, USA, 1983; ISBN 978-1-62949-000-7.

49. Heinson, G.S.; Direen, N.G.; Gill, R.M. Magnetotelluric Evidence for a Deep-Crustal Mineralizing System beneath the Olympic Dam Iron Oxide Copper-Gold Deposit, Southern Australia. *Geology* **2006**, *34*, 573–576. [CrossRef]

50. Graham, S.; Pearson, N.; Jackson, S.; Griffin, W.; O'Reilly, S.Y. Tracing Cu and Fe from Source to Porphyry: In Situ Determination of Cu and Fe Isotope Ratios in Sulfides from the Grasberg Cu–Au Deposit. *Chem. Geol.* **2004**, *207*, 147–169. [CrossRef]

51. Seo, J.H.; Lee, S.K.; Lee, I. Quantum Chemical Calculations of Equilibrium Copper (I) Isotope Fractionations in Ore-Forming Fluids. *Chem. Geol.* **2007**, *243*, 225–237. [CrossRef]

52. Maher, K.C.; Larson, P.B. Variation in Copper Isotope Ratios and Controls on Fractionation in Hypogene Skarn Mineralization at Coroccohuayco and Tintaya, Peru. *Econ. Geol.* **2007**, *102*, 225–237. [CrossRef]

53. Ikehata, K.; Notsu, K.; Hirata, T. Copper Isotope Characteristics of Copper-Rich Minerals from Besshi-Type Volcanogenic Massive Sulfide Deposits, Japan, Determined Using a Femtosecond LA-MC-ICP-MS. *Econ. Geol.* **2011**, *106*, 307–316. [CrossRef]

54. Markl, G.; Lahaye, Y.; Schwinn, G. Copper Isotopes as Monitors of Redox Processes in Hydrothermal Mineralization. *Geochim. Cosmochim. Acta* **2006**, *70*, 4215–4228. [CrossRef]

55. Liu, S.A.; Huang, J.; Liu, J.; Wörner, G.; Yang, W.; Tang, Y.-J.; Chen, Y.; Tang, L.; Zheng, J.; Li, S. Copper Isotopic Composition of the Silicate Earth. *Earth Planet Sci. Lett.* **2015**, *427*, 95–103. [CrossRef]

56. Zhang, C. Research on Metamorphism and Mineralization Geochemistry of the Hongnipo Ore Block of Lala Copper Deposit at Huili, Sichuan Province. Master's Thesis, Chengdu University of Technology China, Chengdu, China, 2019. (In Chinese with English Abstract)

57. Chen, H.S.; Ran, C.Y. *Isotope Geochemistry of Copper Deposits in Kangdian Axis*, 1st ed.; Geological Publishing House: Beijing, China, 1992; pp. 56–57. (In Chinese)

58. Shentu, B.Y. Geological and Geochemical Characteristics and Ore-forming Model of the Lala Copper Deposit in Huili, Sichuan. *Tethyan Geol.* **1997**, *21*, 115–130. (In Chinese)

59. He, D.F. Petrology and Geochemistry of Lala Copper Deposit, Sichuan Province. Ph.D. Thesis, University of Science and Technology of China, Beijing, China, 2009. (In Chinese with English Abstract).

60. Zhu, Z.M. Lala Iron Oxide Copper Gold Deposit: Metallogenic Epoch and Metal Sources. Ph.D. Thesis, Chengdu University of Technology, Chengdu, China, 2011. (In Chinese with English Abstract)

61. Li, W.; Jackson, S.E.; Pearson, N.J.; Graham, S. Copper Isotopic Zonation in the Northparkes Porphyry Cu–Au Deposit, SE Australia. *Geochim. Cosmochim. Acta* **2010**, *74*, 4078–4096. [CrossRef]

62. Larson, P.B.; Maher, K.; Ramos, F.C.; Chang, Z.; Gaspar, M.; Meinert, L.D. Copper Isotope Ratios in Magmatic and Hydrothermal Ore-Forming Environments. *Chem. Geol.* **2003**, *201*, 337–350. [CrossRef]

63. Mathur, R.; Ruiz, J.; Casselman, M.J.; Megaw, P.; Van Egmond, R. Use of Cu Isotopes to Distinguish Primary and Secondary Cu Mineralization in the Cañariaco Norte Porphyry Copper Deposit, Northern Peru. *Miner. Depos.* **2012**, *47*, 755–762. [CrossRef]

64. Tang, D.; Qin, K.; Su, B.; Mao, Y.; Evans, N.J.; Niu, Y.; Kang, Z. Sulfur and Copper Isotopic Signatures of Chalcopyrite at Kalatongke and Baishiquan: Insights into the Origin of Magmatic Ni-Cu Sulfide Deposits. *Geochim. Cosmochim. Acta* **2020**, *275*, 209–228. [CrossRef]

65. Rodriguez-Mustafa, M.A.; Simon, A.C.; Bilenker, L.D.; Bindeman, I.; Mathur, R.; Machado, E.L.B. The Mina Justa Iron Oxide Copper-Gold (IOCG) Deposit, Peru: Constraints on Metal and Ore Fluid Sources. *Econ. Geol.* **2022**, *117*, 645–666. [CrossRef]

66. Hitzman, M.W.; Oreskes, N.; Einaudi, M.T. Geological Characteristics and Tectonic Setting of Proterozoic Iron Oxide (Cu-U-Au-REE) Deposits. *Precambrian Res.* **1992**, *58*, 241–287. [CrossRef]

67. Su, Z.K.; Zhao, X.F.; Li, X.C.; Zhou, M.F. Using elemental and boron isotopic compositions of tourmaline to trace fluid evolutions of IOCG systems: The worldclass Dahongshan Fe Cu deposit in SW China. *Chem. Geol.* **2016**, *441*, 265–279. [CrossRef]

68. Su, Z.K.; Zhao, X.F.; Li, X.C.; Zhou, M.F.; Kennedy, A.K.; Zi, J.W.; Spandler, C.; Yang, Y.H. Unraveling mineralization and multistage hydrothermal overprinting histories by integrated in situ U-Pb and Sm–Nd isotopes in a Paleoproterozoic breccia-hosted IOCG deposit, SW China. *Econ. Geol.* **2021**, *116*, 1687–1710. [CrossRef]